

Winds of Massive Stars

*A numerical investigation of the effects of mass loss
on the evolution of massive stars*



Joris Josiek

Department of Astronomy

University of Geneva

A thesis presented for the degree of

Master of Science (M. Sc.)

supervised by Dr. Sylvia Ekström

submitted on 22 May 2023

Versoix, Switzerland

This thesis was typeset in a template created by the author using the L^AT_EX typesetting system originally developed by Leslie Lamport, based on T_EX created by Donald Knuth. The headings and body are rendered in the *MLModern* font developed by B. Jackowski, J. Nowacki and D. Miller and made available for public distribution and licensed under the L^AT_EX Public Project License.

ACKNOWLEDGEMENTS

It has been almost exactly one year and eight months since I first stepped through the doors of the Geneva Observatory. Having spent the previous three semesters in pandemic-induced isolation, I eagerly welcomed the Observatory as my new daytime home and I would now like to express my appreciation for all the people I have met here, without whom my studies would have at the very least been a lot less enjoyable. Firstly, an enormous thank you to Sylvia for sparking my interest in massive stars research and for being a positive guiding force in my development as an aspiring scientist. I am grateful for all the time and effort you have dedicated to me during this past year and a half, enriching me through our weekly discussions, writing me recommendation letters, taking me to meetings, and being a genuinely good-natured and approachable person. I look forward to our continuing collaboration! I would then like to thank Daniel Schaerer and François Bouchy for all their work organizing and coordinating the Master program in astrophysics. It is possible that I would not have found my way to astronomy without the existence of a dedicated, well-structured and well-advertized course such as this one. I am grateful to Andreas Sander for useful discussions regarding this work, and for his relentless effort and dedication in finding a way to offer me a PhD position in his group. Thanks to him I now have the chance to explore my interest in massive stars, their evolution and their atmospheres for at least a further three years in Heidelberg. I thank Eoin Farrell and Anne Verhamme for being part of the jury for this thesis. I appreciate the time you are taking out of your schedules in order to read, hear and evaluate my work, and I hope that it may offer you at least a little bit of enjoyment in return. I am deeply appreciative of my parents for making it possible for me to go on this adventure for almost two years, and for constantly supporting and helping me in the background. You have contributed greatly to reducing my stress and making my experience go as smoothly as possible. Finally, I consider myself extremely lucky to have met such an incredible group of friends in the Master's programme, who have always been available to fill my life with excitement, joy and unforgettable experiences. I will very fondly remember our day trips exploring the beautiful region around Geneva by train, car and bike, our group travel adventures to Venice and Lisbon, our chill hangouts, and especially our semesterly international lunches (feasts). Last but not least, I am grateful to you, Mariam, for being a constant support figure in my life. I can always rely on you to know what I need and to take over when I am too tired to carry on. I appreciate that you are always there for me when I need you.

ABSTRACT

Stellar winds constitute one of the most important drivers of massive star evolution, and they are a vital source of chemical, mechanical and radiative feedback on the galactic scale. Despite its significance, mass loss still remains a major uncertainty in stellar models and it is therefore of essential importance to study its role in stellar evolution and the effect it can have on observable phenomena. In this work, I aim to examine the impact of main sequence mass loss on the structure of massive stars throughout their entire evolution. Using the Geneva stellar evolution code (GENEC), I compute grids of single, non-rotating stellar models at solar metallicity of initial masses between 20 and 120 solar masses, with three different mass loss rate prescriptions for main sequence as well as two different prescriptions for the red supergiant (RSG) phase. From this I obtain detailed numerical predictions regarding the structure and evolution of massive stars, and infer the role of main sequence mass loss by comparison of the various prescriptions. We conclude that main sequence winds may considerably shape the structure of evolved stars, despite these being much weaker than winds experienced in the later evolutionary phases. Furthermore, the results show several distinct evolutionary paths for massive stars which are significantly influenced by the chosen mass loss rates, both in the main sequence and the red supergiant phase. We discuss the impact of these results as well as their limitations within the broader context of stellar evolution modeling and observation.

DECLARATION

I hereby declare that I have produced this thesis independently under the supervision of the Department of Astronomy of the University of Geneva without the help of third parties, and that I am its sole author. Furthermore, I declare that no sources or learning aids, other than those listed, have been used.

Versoix, 22 May 2023

Place, Date



Joris Josiek

CONTENTS

List of Tables	vi
List of Figures	vii
Glossary of Abbreviations	ix
1 Introduction	1
1.1 Motivation	1
1.2 Context	2
1.3 Project goals and overview	3
2 Stellar evolution	4
2.1 What is a star and why does it evolve?	4
2.2 Evolution in the core	5
2.3 Evolution on the surface	8
2.4 Stellar death	9
2.5 A note about spectral types	10
3 Stellar modeling	11
3.1 Equations of stellar structure and evolution	11
3.2 Mass loss prescriptions	13
3.3 The Geneva stellar evolution code	16
3.4 Definition of the model grid	17
4 Predictions of the models	18
4.1 Characterization of the mass loss prescriptions	18
4.2 Main sequence evolution	22
4.3 Formation and evolution of Wolf-Rayet stars	31
4.4 Supernova progenitors	37
4.5 Stellar populations	41
5 Conclusion	44
5.1 Summary	44
5.2 Discussion and Outlook	45
A Data tables	54
B Analytical derivation of stellar scaling relations	59

LIST OF TABLES

3.1	Summary of the models computed with GENEC for the present study. Models marked with (†) did not complete central carbon burning.	17
4.1	Best fit parameters for the power law relating average mass loss during the main sequence to the initial mass. Parameter a represents the characteristic $\log \dot{M}$ of a $20 M_{\odot}$ star, and b is the exponent of the relation.	21
4.2	Best fit parameters of the linear fits relating the TAMS mass to the initial mass in the different mass loss regimes	22
4.3	Evolutionary definition of WR subtypes.	32
4.4	Relative abundances of different types of stars in a population of stars of initial masses 20–120 M_{\odot} using different mass loss rates, assuming the IMF from Salpeter (1955) and constant SFR.	42
A.1	Time-averaged mass loss rates obtained during the validity domains of the \dot{M}_{OB} prescriptions (main sequence only), as well as the \dot{M}_{RSG} prescriptions, with standard deviations. Units of mass loss rates are solar masses per year. This data shown in Figure 4.2 and Figure 4.3	55
A.2	Properties of the models at the terminal-age main sequence (TAMS), discussed in section 4.2	56
A.3	Properties of the models when they enter the Wolf-Rayet (WR) phase, as shown in Figure 4.12	57
A.4	Properties of the models at the end of central carbon burning, discussed in section 4.4 , with data shown in Figure 4.14 , Figure 4.15 , Figure 4.16 and Figure 4.17	58

LIST OF FIGURES

2.1	Schematic of the two main mechanisms for the fusion of hydrogen to helium. Black symbols and text show the transformations of the nuclides, blue arrows labeled with the letter p denote proton captures, red arrows labeled with e^+ denote positron decay. In (b), the ejection of the ${}^4\text{He}$ nucleus is shown by a circled yellow “ α ”. . . .	5
2.2	Schematic depiction of the different pathways for the apparent evolution of massive stars. Arrows show the different possible transitions according to stellar models . .	9
4.1	Time fraction of the main sequence spent within the validity domain of the chosen \dot{M}_{OB} prescription.	19
4.2	Time-averaged logarithm of the mass loss rate as a function of initial mass for the three O/B mass loss prescriptions, with power-law fits.	20
4.3	Time-averaged logarithm of the mass loss rate as a function of initial mass for the two RSG mass loss prescriptions. The shapes of the data points correspond the \dot{M}_{OB} prescription as in Figure 4.2	20
4.4	TAMS mass as a function of initial mass for the three \dot{M}_{OB} prescriptions, with regime-wise linear fits.	23
4.5	Main-sequence evolution of the Eddington parameter for selected models using the Bes20 \dot{M}_{OB} prescription. The horizontal dotted line marks the transition between the optically thin and optically thick wind regime.	23
4.6	Mass-luminosity relation for the models at the TAMS	24
4.7	Hertzsprung-Russell diagram showing the evolutionary tracks of selected models during the main sequence. Additionally, dotted curves represent the location of the models at various central hydrogen mass fractions X_c as markers for evolutionary progress.	25
4.8	Main-sequence evolution of the convective core mass for selected models.	26
4.9	Snapshots of the abundance profile of the 60 M_{\odot} model with Bes20 at different moments of the MS ($X_c = 0.7, 0.5, 0.3, 0.1$), showing the internal distribution of hydrogen and helium as a function of the radial mass coordinate. The shaded gray area shows the extent of the convective core, with the shaded yellow area representing the envelope.	27
4.10	Evolution of surface hydrogen abundance as a function of relative mass lost for models with initial masses (a) 30 M_{\odot} (with Cro01 \dot{M}_{RSG}), (b) 60 M_{\odot} , (c) 85 M_{\odot} . The horizontal dotted line shows the threshold of $X_s = 0.3$ as the definition of WR stars. The plotted shapes mark the location of the TAMS on each model.	29
4.11	Schematic hydrogen depletion curve depicting the characteristic zones.	31
4.12	Corner plot of model parameters at the point of WR formation. The colors and shapes indicate the \dot{M}_{OB} prescription. Models that have an RSG phase use the Cro01 \dot{M}_{RSG} prescription.	33

4.13	Full evolution in the HRD for models with initial masses (a) $30 M_{\odot}$ (with Cro01 \dot{M}_{RSG}), (b) $60 M_{\odot}$, (c) $85 M_{\odot}$. The plotted shapes mark the beginning of the WR phase on each model.	36
4.14	HRD showing the evolutionary endpoints of the models that were computed until the end of core carbon burning. Labeled ellipses show different populations of supernova progenitors.	38
4.15	Final mass of the models as a function of initial mass.	39
4.16	Total mass lost in the models after the main sequence as a function of initial mass. The models separate into groups depending on which phase dominates the post-MS mass loss.	39
4.17	Mass of the CO core (whose boundary is defined as the layer where helium abundance increases above 1% when starting from the center outwards) at the end of central carbon burning. For models with an RSG phase, the results from both \dot{M}_{RSG} prescriptions are shown, but their final core masses are so similar regardless of the mass loss prescriptions that the scatter points are indistinguishable.	40
4.18	Cumulative timescales of the post-MS evolutionary phases as a function of initial mass for different combinations of \dot{M}_{OB} and \dot{M}_{RSG} prescriptions. The x -axis is scaled using an initial mass function so that the area of each region is proportional to the fraction of stars in the corresponding phase in a population of constant star-formation rate. (See main text for details.) The dashed white lines represent the approximate location of the boundary between the low mass loss regime and the high mass loss regime of the MS, according to Figure 4.4	42

GLOSSARY OF ABBREVIATIONS

BH	Black hole
BSG	Blue supergiant
EOS	Equation of state
GENEC	Geneva stellar evolution code
HRD	Hertzsprung-Russell diagram
ISM	Interstellar medium
LMC	Large Magellanic Cloud
MS	Main sequence
RSG	Red supergiant
SFR	Star formation rate
SMC	Small Magellanic Cloud
SN(e)	Supernova(e)
TAMS	Terminal-age main sequence
WR	Wolf-Rayet
YSG	Yellow supergiant
ZAMS	Zero-age main sequence

PHYSICAL CONSTANTS

The following is a list of all physical constants used in this work.

Symbol	Value	Unit (SI)	Description
c	2.99792458×10^8	m s^{-1}	Speed of light in a vacuum
k	1.380649×10^{-23}	$\text{m}^2 \text{kg s}^{-2} \text{K}^{-1}$	Boltzmann constant
σ	5.67051×10^{-8}	$\text{W m}^{-2} \text{K}^{-4}$	Stefan-Boltzmann constant
m_u	1.660539×10^{-27}	kg	Atomic mass constant (1/12 of the mass of the carbon nucleus)
G	6.6743×10^{-11}	$\text{N m}^2 \text{kg}^{-2}$	Gravitational constant
M_\odot	1.989×10^{30}	kg	Solar mass
L_\odot	3.828×10^{26}	W	Solar luminosity
Z_\odot	0.014	–	Solar metallicity

CHAPTER 1

INTRODUCTION

1.1 Motivation

Humans have been studying stars for a long time. Early records show that people living in Mesopotamia around 1000 BCE were already systematically documenting the apparent motions of stars in the sky (ESA Science & Technology, 2019), which is something we continue to do today, albeit on a much larger scale (Gaia Collaboration, 2021).

Humanity has had such a consistent fascination with stars in the past, that I find it not unreasonable to postulate that we have been wondering about them for pretty much as long as we have been able to wonder. Stars have certainly had a profound influence on human civilizations throughout recorded history, and many significant revolutions in society can be attributed to them, for instance the ability to navigate across oceans, track time and create calendars. It is quite possible that our primordial urge to answer life's big questions was what made astronomy one of the first scientific disciplines to arise, and although our philosophy around science has changed much within the course of the past millenia, even now we are still motivated by our fundamental curiosity of understanding how the universe works.

Within the last few centuries, as astronomy shifted more and more towards astrophysics, scientists began to focus more on studying the fundamental physical principles governing the cosmos, and with ever-improving observational techniques, significant developments were made in our understanding of the universe. Arguably one of the most important advances was becoming aware our own place in the universe by showing that the sun is really just an ordinary star among billions of others, and that there is therefore nothing remotely special about us.¹ This is actually an idea that dates back to ancient Greece but remained for millenia nothing more than an abstract philosophy until distance measurements and spectroscopy allowed us to prove that the sun indeed has a similar size, brightness and chemical composition to other stars.

Today, we still don't really understand stars.² Granted, we are a lot more knowledgeable than we were a thousand years ago, and we have figured out a lot about what stars are, how they look, how they live and how they interact with each other and other objects. But when it comes to specific details, especially concerning stars that are much more massive and more extreme than our own sun, there are still many mysteries left to solve. For one, being able to accurately explain and predict the characteristics of the stellar populations we observe is no easy task, since it requires an intricate understanding of all the mechanisms that play a role in determining how stars evolve

¹Except perhaps for the ability to write this sentence.

²Fortunately.

and hence how they will appear in space.

With the help of computer simulations, we are now able to study stars much more closely than we ever could by observing them in reality. The significant advantage of simulations is having full control over the system we want to investigate, as well as full knowledge of its properties. Given sufficiently accurate input physics, we obtain the ability to isolate and study the effects of any physical phenomenon on the structure and evolution of stars just by varying the ingredients of the simulations and looking at the outcome. This use of computational modeling constitutes a large part of current stellar evolution research, including the work you are about to read.

1.2 Context

The general evolution of massive stars is well-known, taking place more or less as will be described in [Chapter 2](#): A star is born from a collapsing cloud of gas and begins to fuse hydrogen in its core. Once the core has exhausted its fuel, it contracts and generates heat which is used in part to ignite the next phase of nuclear burning, and in part to inflate the envelope of the star, which then lives the rest of its life as some kind of supergiant, perhaps becoming a more exotic kind of star known as a Wolf-Rayet³ star at some point. At the end, the chain of nuclear fusion breaks, the stellar core collapses, and material is scattered in a supernova explosion.

Alas, this level of depth is not sufficient for most applications of massive star evolution research. On the large scale, massive stars retain a vital importance for understanding the structure and evolution of galaxies, since their powerful winds and high ionizing flux play a direct role in shaping the physical and chemical structure of their surroundings ([Krause et al., 2013](#)). Unfortunately, massive stars are greatly outnumbered by their low-mass counterparts, because they form more rarely and have a much shorter lifespan ([Salpeter, 1955](#)). This makes it much more difficult to perform large population surveys of them, and many phenomena related to massive stars are so rare that we only have a handful of observations. For instance, the number of Wolf-Rayet stars discovered to date is counted in the hundreds ([Massey et al., 2014](#); [Mauerhan et al., 2011](#)), an incredibly small number compared to the billions of stars we know in total ([Gaia Collaboration, 2021](#)).

The astrophysics community relies greatly on numerical models to obtain a complete picture of massive star populations and their impact that is currently unattainable by observations alone. However, the ingredients of stellar models come from a wide range of complex physics such as hydrodynamics, radiative transport, thermodynamics, magnetism, atomic physics and gravity, which must be radically simplified in order to make any computation feasible, either because an accurate treatment would be too computationally expensive or because a particular mechanism is not yet understood well enough to implement anything more detailed than a general approximation.

Arguably one of the most important ingredients in stellar models is mass loss. Within the course of their lives, massive stars can eject more than half of their own initial mass in the form of stellar winds, which not only transfer energy and momentum into the interstellar medium (ISM), but also feed it with new gas that has perhaps been chemically altered. Through mass loss, stars also change their own appearance as they progressively remove layers from their surface. This can have profound impacts on a star’s own evolution, possibly reaching all the way into the core. In general, there is complicated feedback between stellar evolution and mass loss, as these two processes constantly influence each other. Despite their significance, winds of massive stars are still poorly constrained. Numerous different methods have been proposed to measure, calculate and

³The definition of this term will be introduced and discussed more in [Chapter 2](#), but for now, I ask the reader to accept that it is a rare kind of massive star that is very important and exciting to study.

predict the mass loss rate of stars (e.g. [Vink, 2022](#)), each with their own caveats and uncertainties, mostly caused by the fact that mass loss is generally not constant and symmetrical as assumed by models, but is rather a highly turbulent and chaotic process.

In stellar evolution codes, mass loss is typically implemented in the form of simple equations, called *prescriptions* or *recipes*, describing the mass loss rate from the surface as a function of a few macroscopic stellar parameters such as luminosity, surface temperature and chemical composition. A single prescription is usually only applied for a specific evolutionary phase where the star falls into the validity domain of the prescription, resulting in a total of up to five different prescriptions being applied during the evolution of a massive star (e.g. [Ekström et al., 2012](#)). Equations for the mass loss rate can be derived from empirical, theoretical or numerical considerations, or combinations thereof, and since such a large variety of them have been proposed, it is important to investigate the effects that arise when applying them in an evolution model. These investigations are beneficial for two reasons. Firstly, they allow us to test and constrain the validity of various prescriptions with respect to observational data, perhaps offering us deeper insight into how the mechanisms of stellar winds function in reality. Secondly, with no regard for the level of ‘truth’ in any particular mass loss prescription, experimenting with different mass loss rates in models allows us to investigate the effect that mass loss has on stellar evolution, allowing us to understand how it may possibly relate to various phenomena we observe.

1.3 Project goals and overview

In this work, I investigate three mass loss prescriptions for hot massive stars, and two prescriptions for cool massive stars, of which some are recent proposals and others are a commonly used standard. I implement the new equations into the Geneva stellar evolution code (GENEC) and apply them in a series of evolution models of stars of different masses and analyze the results. The main goals of this project are:

- to study the effects that main sequence mass loss has on the entire evolution of massive stars and their populations, including supernova progenitors and remnants,
- to compare the impact of main sequence mass loss with the impact of mass loss during the later phases of evolution,
- to discuss the influence of mass loss on the formation, structure and evolution of Wolf-Rayet stars, and
- to evaluate the benefits and limitations of the different mass loss prescriptions for reproducing observable and observed effects.

I will begin by reviewing some background on stellar evolution in [Chapter 2](#), which will introduce the necessary terminology for discussing the results of the models in later chapters. [Chapter 3](#) is dedicated to the process of obtaining stellar evolution models. Here, I will give an overview of GENEC and discuss the various physical ingredients with a focus on mass loss. I will also define the parameter space explored in this study. In [Chapter 4](#), I will present the main results of the models and analyze them with respect to the above research goals. Finally, I will draw conclusions from the results and discuss the impact and limitations of this work in [Chapter 5](#).

CHAPTER 2

STELLAR EVOLUTION

2.1 What is a star and why does it evolve?

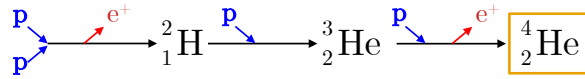
The word “star” has historically had a very broad definition. Thousands of years ago, virtually any object visible in the sky other than the moon and the sun was called a star. At some point, some scholars in ancient Greece noticed that some of those stars were moving considerably compared to most others, so they called them “wandering stars”, or in ancient Greek: *plánetes astéres*. A new category of objects was born. As more and more new types of objects were discovered throughout the centuries, what we call a star has become much more restrictive, although its Greek cognate “astro-” has retained its general meaning referring to anything in space.

In a scientific context today, a star is a sphere of gas that is sustained by nuclear fusion in its core. Since nuclear fusion can only take place in a high-temperature and high-pressure environment, a star must by definition reach a certain mass threshold in order to generate such conditions. This minimum mass is around $0.08 M_{\odot}$,¹ determined both by numerical models (Chabrier & Baraffe, 1997) and observational constraints (Richer *et al.*, 2006). The maximum mass that a star can have is much more vague and seems to depend a lot on its chemical composition, at least in theory. Observationally, the most massive stars we know could be up to $250 M_{\odot}$, although these estimates carry large uncertainties (Wu *et al.*, 2016).

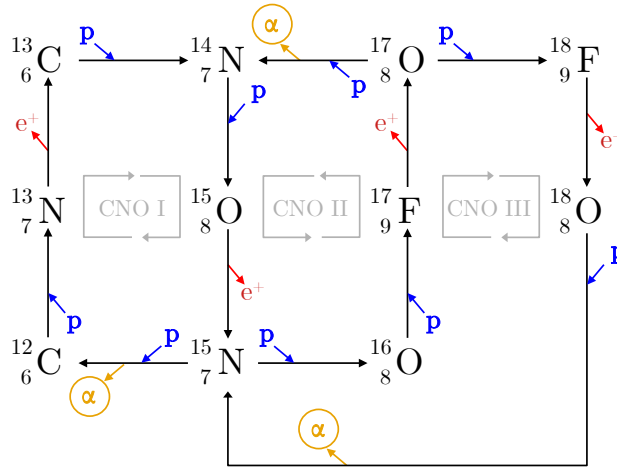
Most stars consist mainly of hydrogen and helium, a fact that went considerably against the scientific mainstream of the time when it was discovered by Cecilia Payne-Gaposchkin (1900–1979) in her PhD thesis (Payne, 1925). It eventually became known that those elements are not only the most abundant ones in stars, but in the whole universe. In fact, the primordial universe contained almost *exclusively* hydrogen and helium, and all heavier elements were only later created through nuclear fusion in stars.

The process of creating heavier elements by fusing the atomic nuclei of lighter elements is known as *nucleosynthesis* and it is the primary driver of evolution in stars. While it progressively changes the chemical and physical structure of stars, it generates the energy required to sustain the star against its own gravity for long periods of time. Throughout its life, a star will go through multiple distinct phases of evolution, both in terms of its interior fusion processes as well as its external appearance.

¹ $1M_{\odot} \approx 2 \times 10^{30}$ kg is mass of the sun, or “solar mass”. It is the typical unit of mass used in stellar evolution.



(a) The pp-chain.



(b) The CNO cycle

Figure 2.1: Schematic of the two main mechanisms for the fusion of hydrogen to helium. Black symbols and text show the transformations of the nuclides, blue arrows labeled with the letter p denote proton captures, red arrows labeled with e^+ denote positron decay. In (b), the ejection of the ${}^4_2\text{He}$ nucleus is shown by a circled yellow “ α ”.

2.2 Evolution in the core

The core is typically the densest and hottest region of a star and therefore offers the ideal environment for nuclear fusion. Consequently, chemical evolution in stars is driven from the center outwards, i.e. heavier elements are first produced in the core and may then be transported outwards by various mixing mechanisms. This eventually results in a typical layered structure where the mean molecular weight (average mass per particle) increases from the surface towards the center. In this section, I review the most important nuclear fusion processes that take place in the stellar core, which ultimately shape the chemical structure of stars. This background can be reviewed more in-depth in textbooks such as [Maeder \(2009\)](#).

Hydrogen is the lightest element and incidentally also requires the least energy to undergo nuclear fusion. Therefore, when a cloud of gas collapses to form a star and its internal pressure and temperature progressively increases, hydrogen burning is the first to ignite.² There are several different chains of nuclear reactions that hydrogen can undergo, all of which lead to the production of the next heaviest element, helium. The simplest possible path is known as the *pp*-chain, shown schematically in [Figure 2.1a](#), where a hydrogen-1 nucleus (a single proton, written as p) will successively capture other protons, converting some to neutrons via β -decay, until a helium-4 nucleus (written as ${}^4_2\text{He}$ or simply as α) forms.

²In stellar evolution, we often use terms like “burning” and “ignition” to refer to nuclear fusion processes. However, the processes are physically very different from a conventional fire resulting from combustion, which refers to a reaction on the molecular level, but where atomic nuclei are not involved.

The two positrons ejected during these reactions quickly annihilate with free electrons to produce more gamma radiation. The *pp*-chain is the dominant mechanism for hydrogen burning in stars less massive than $1.3 M_{\odot}$, but at higher masses a different process known as the CNO-cycle is favored. This mechanism, shown in [Figure 2.1b](#), is a reaction chain that requires trace amounts of carbon, nitrogen and oxygen as catalysts for hydrogen fusion. There are three main branches for this cycle, denoted as CNO I, CNO II and CNO III, each of which contains a chain totaling 4 proton captures and 2 positron decays starting from different nuclides and resulting in the ejection of a helium nucleus.

The CNO cycle is generally not in equilibrium, meaning that each reaction involved does not run at the same rate. While positron decay follows an exponential trend with a fixed half-life, proton capture depends on the availability and energy of external protons, which is directly linked to the thermodynamic conditions of the medium. With time, the abundances of the nuclides adjust towards an equilibrium state, which is particularly rich in ^{14}N . A slightly elevated abundance of nitrogen is therefore regarded as a byproduct of hydrogen burning in massive stars.

Whether through the *pp*-chain or the CNO-cycle, the net result of hydrogen burning is producing one helium nucleus and two positrons from four hydrogen nuclei. Including the subsequent annihilation of the positrons, the total energy released per reaction cycle is 26.7 MeV, some of which is lost to the neutrinos released during positron decay.

The phase during which a star fuses hydrogen to helium in its core is known as the *main sequence* (MS). During this phase, stars usually have a stable structure and show little to no variability. The main sequence is the longest phase of evolution, lasting for around 90% of a star's total lifetime, and therefore most of the stars in the universe (including the sun) are in this phase.

After a star has exhausted the hydrogen fuel in its center, the core stops being sustained by radiation pressure generated by nuclear fusion and therefore contracts under its gravity. The heat produced by this contraction increases the core's temperature until it reaches the threshold at which helium can undergo further fusion. Unless otherwise referenced, the following information on post-main-sequence fusion processes is a summary of key notions that can be reviewed in textbooks such as [Padmanabhan \(2000\)](#) (pp. 581–585) and [Hansen & Kawaler \(1994\)](#) (pp. 242–249).

When two helium-4 nuclei fuse, they produce a nucleus of beryllium-8, which is highly unstable and decays back into two helium-4 nuclei with an extremely short half-life of around 10^{-16} s. However, if the temperature is high enough, the beryllium-8 nucleus can fuse with another helium-4 nucleus quickly enough before it has time to decay. This produces a carbon-12 nucleus in an unstable excited state. Most of these decay back to beryllium, but around 1 in 2500 will relax into the stable ground state by emitting two gamma photons ([Obst & Braithwaite, 1976](#)) and thus, stable ^{12}C starts to accumulate in the star. This mechanism for producing carbon from helium nuclei is known as the *triple-alpha* (or 3α) process. Given a sufficiently high concentration of carbon in the star, some ^{12}C nuclei can fuse with an additional helium nucleus to form stable ^{16}O as a byproduct of helium burning. The precise cross-section of this reaction is still a relevant problem in nuclear astrophysics, and as a key ingredient of stellar evolution models, it represents one of their major uncertainties ([Smith et al., 2021](#)). In general, one can say that this reaction is favored over the 3α reaction at higher temperatures, so massive stars tend to have a higher core oxygen mass fraction at the end of helium burning than low-mass stars.

During core helium burning, the star may keep burning hydrogen in a shell around the core, provided that it still possesses a sufficiently massive envelope above the shell to exert the required pressure for hydrogen burning. Additionally, the core of massive stars is chemically homogeneous during helium burning as well as the main sequence due to convective mixing. During central carbon burning, the core temperature gradient is generally too low to induce convection, and thus

the chemical evolution takes place inhomogeneously, being more rapid at the center. The core may then become convective again during later burning phases. It is also important to note that, under normal conditions, nuclear burning takes place isothermally, i.e. at constant temperature, because of the following thermodynamic negative feedback effect. If the energy production from fusion increased slightly, causing heating of the gas, this heat would generate pressure (assuming an ideal gas), which would expand the gas. This expansion would in turn result in cooling and a decrease in nuclear energy production. This is the stabilizing effect that regulates nuclear burning in stars. Since most nuclear reaction rates are extremely sensitive to temperature ($\sim T^{17}$ for the CNO cycle, $\sim T^{41}$ for 3α), the equilibrium temperature for each burning phase is relatively well-defined.

At the end of core helium burning, the core contracts and heats up again. Low- and intermediate-mass stars are unable to generate the necessary temperature for further fusion and thus their core keeps contracting until it is supported by electron degeneracy pressure, where it remains as a slowly cooling white dwarf for an indeterminate amount of time³. In comparison, stars that begin their main sequence with a mass of at least $8 M_{\odot}$ are expected to reach central temperatures high enough to ignite the fusion of elements heavier than helium in the latter stages of their lives. This is the defining characteristic that places a star in the category of *massive stars*, which will be the sole focus of this work hereinafter.

The post-helium-burning phases of nuclear fusion in massive stars are very short-lived compared to the main sequence and the helium-burning phase: a star will typically only spend around 0.1% of its life burning elements heavier than helium in its core. This is due in part to nuclear fusion becoming less efficient for heavier elements and in part to the higher fractions of energy being lost to neutrinos. Both of these effects reduce the radiation pressure support of the star and cause the core to contract and heat up more and thus burn its fuel more quickly.

There is an extensive network of nuclear reactions that can take place in the interior of an evolved star. After central helium burning, carbon is the next element to ignite in a stellar core, while helium can continue to burn in a shell around the core. During central carbon burning, two ^{12}C nuclei will generally fuse to form a ^{24}Mg nucleus, but can also produce other atomic species, notably ^{23}Na through proton ejection and ^{20}Ne through alpha ejection. In general, there are many secondary reactions involved in the late burning phases that can produce a wide variety of elements in the periodic table through the exchanges of protons, neutrons and alpha particles, as well as electron capture and β -decay. At the end of central carbon burning, the dominant species are typically ^{16}O , ^{20}Ne and ^{24}Mg , with trace amounts of other isotopes of neon and magnesium, as well as some sodium.

After central carbon burning, there is a short phase of neon photodisintegration, where some of the built-up ^{20}Ne undergoes alpha decay back to ^{16}O due to stimulation by an absorbed photon. After this phase, the core is hot enough to undergo oxygen burning, which forms mainly ^{28}Si and notable amounts of sulfur and calcium. After oxygen burning, there are no more reactions involving the fusion of two heavy nuclei. Instead, successive capture of alpha particles allows the silicon (among other nuclides) to be transformed into a chain of heavier elements⁴, ending with the synthesis of ^{52}Fe and ^{56}Ni . These isotopes of iron and nickel have the highest binding energy per nucleon of all nuclides, and thus the production of even heavier elements is no longer exothermic. Therefore, stars that have accumulated an iron-nickel core lose their energy source and are nearing the end of their evolution.

³Certainly much longer than the current age of the universe.

⁴This phase of evolution is often referred to as silicon “burning”, although it is distinct from the other central burning phases in that it does not involve silicon nuclei fusing with each other.

2.3 Evolution on the surface

While stars go through the various phases of evolution in their core, their upper layers also evolve in distinct observable phases, which are characterized by periods of contraction and expansion (corresponding to heating and cooling, respectively). Additionally, stellar winds consistently eject material from the surface into the ISM and progressively uncover deeper layers within the star. Stellar mass loss is caused mainly by radiation pressure from the interior, which becomes significant for highly luminous massive stars, for which the mass loss rate can reach $10^{-5} M_{\odot} \text{ yr}^{-1}$ in the main sequence and up to $10^{-2} M_{\odot} \text{ yr}^{-1}$ for part of the later stages. This makes mass loss one of the most important drivers in the evolution of massive stars. For comparison, the sun only loses around 10 quadrillionths (10^{-14}) of its mass per year in the form of solar winds.

Given sufficiently long timescales, surface and core processes may affect each other through various feedback mechanisms between the two regions, some of which will also be explored as part of this work. For this reason, the surface evolution is mostly synchronized with the core evolution in the early life of a star, but can be completely disconnected in the later phases because of shorter phases of core nuclear burning.

At the surface, the appearance of a star is described mainly by three macroscopic parameters, namely its luminosity L , effective temperature⁵ T_{eff} and the stellar radius R . The parameters are related via the Stefan-Boltzmann law for the radiation of a spherical black body, as follows:

$$L = 4\pi R^2 \sigma T_{\text{eff}}^4 \quad (2.1)$$

At the beginning of the main sequence, a point in time commonly referred to as the *zero-age main sequence* (ZAMS), young stars are hot and compact. Stars more massive than $20 M_{\odot}$ start from this point with a radius around 5 to 15 times the sun’s and surface temperatures between 35 000 K and 55 000 K. At these temperatures, stars appear bluish-white in color and are of the spectral type O, though they may slowly cool and finish their main sequence as B-type stars. (See [section 2.5](#) for some background on spectral classification of stars.)

After the end of the main sequence (*terminal-age main sequence* or TAMS), the stellar envelope suddenly receives a surge of thermal energy from the contracting core, causing an expansion on a relatively short timescale of a few thousand years. This expansion causes the surface to cool to around 4 000 K where the star appears more reddish in color. In this inflated state, a massive star is known as a red supergiant (RSG). A famous example of a star currently in this phase is Betelgeuse, which can be found in the Orion constellation. A large convective zone may form at the base of a RSG’s envelope due to the high temperature gradient, causing a dredge-up of H-burning products towards the upper layers of the star.

The subsequent evolution after the RSG phase depends entirely on the mass loss rate experienced by the star in this state, which is currently poorly constrained. Strong mass loss tends to reveal deeper and hotter layers of the star, which consequently evolves “back to the blue” becoming a yellow supergiant (YSG) or blue supergiant (BSG), whereas weak mass loss can cause the star to remain in the RSG phase for the rest of its evolution. However, the full picture is much more complex, since a delicate interplay of mass loss and various expansion and contraction processes can cause multiple bouts of blueward and redward evolution during the late phases of a star’s life.

Aside from temperature, mass loss also importantly impacts the chemical composition of the stellar surface since it causes the exposure of deeper layers that are enriched with products of nuclear burning and depleted of hydrogen. If mass loss is strong enough, stars are able to evolve towards a

⁵The effective temperature is also known as the surface temperature.

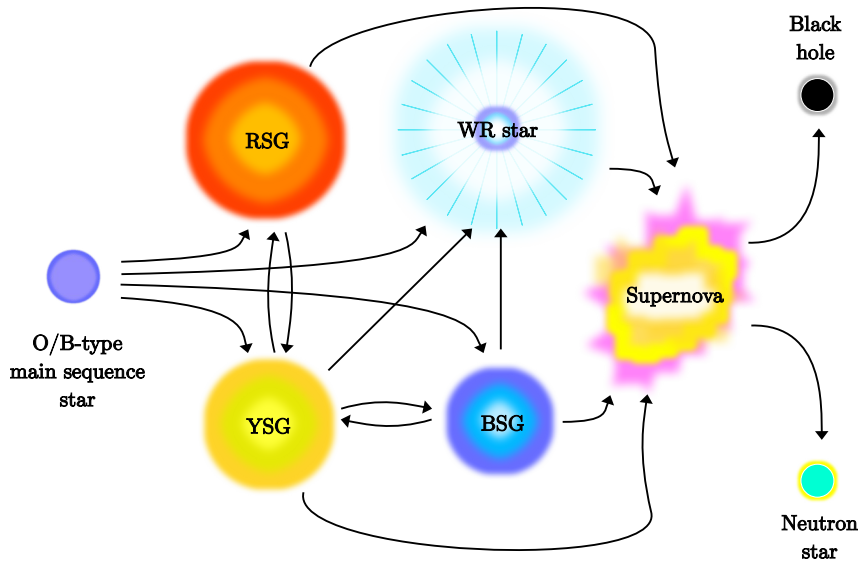


Figure 2.2: Schematic depiction of the different pathways for the apparent evolution of massive stars. Arrows show the different possible transitions according to stellar models

class of objects known as *Wolf-Rayet* (WR) stars, defined spectroscopically as stars showing broad emission lines and signatures of an optically thick stellar wind, i.e. where the star itself is obscured by the material it ejects. In theoretical stellar evolution research where stellar spectra are not available, WR stars are defined as having a high surface temperature of above 10 000 K, and low surface hydrogen mass fraction, typically below 30–50% (in this work I use 30% as the defining threshold). Essentially, they are hot stripped stars. This theoretical definition of WR stars based on macroscopic stellar parameters is thought to be closely related to their spectroscopic definition, although significant discrepancies can arise and indeed become problematic for the study of such objects, especially when aiming to compare models with observations.

Stars initially more massive than approximately $40 M_{\odot}$ generally don't cool down enough to become RSGs during their post-MS expansion, and may evolve to yellow supergiants, blue supergiants or even Wolf-Rayet stars directly from the main sequence. Generally, a number of different evolutionary paths are possible for massive stars, a summary of which is shown schematically in Figure 2.2. It shows that the post-main sequence evolution of massive stars can be very convoluted, in part due to mechanisms whose origin and effects are not yet understood in intricate detail, most notably mass loss.

2.4 Stellar death

A massive star finishes its evolution when its source of energy is depleted, i.e. when nuclear fusion is no longer exothermic, corresponding to an accumulation of iron and nickel in the core. Within a matter of seconds, the core loses support from radiation pressure and violently collapses under its own gravity, sending powerful shockwaves through the star causing it to disintegrate in an explosion that is momentarily more luminous than an entire galaxy. This phenomenon is known as a core-collapse supernova (SN)⁶, which is thought to be the ultimate fate of most massive stars. The remaining core is compressed to extremely high densities, and becomes a neutron star or a black hole depending on its mass. SNe are so energetic that they induce the fusion of elements

⁶Plural: supernovae (SNe)

even heavier than iron and they are to date the only known cosmic events with this ability. They distribute metal-enriched material into the neighboring ISM (as far as several lightyears), which can later be recycled for new star formation. It is unclear whether all massive stars ultimately die as a supernova, and a direct ‘silent’ collapse into a black hole is also considered as a possible alternative scenario for the death of the most massive stars (Smartt, 2009).

2.5 A note about spectral types

We have already encountered references to the so-called spectral classification of stars in some of the previous sections. Essentially, stars are categorized into different spectral types depending on the features that are visible in their observed spectral energy distribution, which are usually absorption lines of various chemical species. These lines are formed in the upper layers of the star due to atoms and ions absorbing light of certain wavelengths corresponding to electronic transitions between quantized energy levels. The observed line strengths are thus a direct consequence of the distribution of electrons into both free and bound states, which is closely related to the temperature of the system (See Boltzmann distribution and Saha equation). A direct correspondance therefore exists between spectral type and surface temperature. From hot to cold, the standard spectral types of stars are named O, B, A, F, G, K, and M. In addition to this, several “special” spectral types exist for stars that exhibit unusual spectral features, for example Wolf-Rayet stars.

As previously mentioned, it is important to note that only a stellar spectrum (from observations or simulations) can be used to directly infer a spectral type. In a stellar evolution model which does not provide a detailed spectrum, we can infer a “theoretical” spectral type based on proxies such as effective temperature and surface abundances. In this case, there may be discrepancies between observational and theoretical definitions, the consequences of which must be raised as part of the scientific discussion.

Whenever I refer to stars by their spectral type in this work, I tacitly imply the theoretical definition, unless explicitly stated otherwise. Most commonly, this will be for stars of type O ($T_{\text{eff}} \geq 25\,000\text{ K}$) and type B ($10\,000\text{ K} \leq T_{\text{eff}} < 25\,000\text{ K}$), as well as for Wolf-Rayet stars as defined in the relevant sections.

CHAPTER 3

STELLAR MODELING

3.1 Equations of stellar structure and evolution

3.1.1 Equations of stellar structure

Ignoring rotation, a star can be approximated as a spherically symmetric object whose geometrical center corresponds to its center of gravity. As such, it can be modeled simply by a set of one-dimensional functions describing its various properties along the radial axis. The most fundamental ingredient of a stellar structure model is a set of equations, aptly named the equations of stellar structure, which describe the macroscopic physics relating different properties of a star. Together with a set of boundary conditions, these equations uniquely yield a solution for the stellar structure in dynamical equilibrium.

The first equation of stellar structure is the equation of **mass continuity**. Via the density profile $\rho(r)$, it relates the radial distance r to the radial mass M_r , a quantity that corresponds to the mass enclosed by a sphere of radius r centered on the star.

$$\frac{dM_r}{dr} = 4\pi r^2 \rho \quad (3.1)$$

When studying the stellar structure, it is often more useful to parametrize with M_r as the radial coordinate instead of r , since this allows us to track the physical mass in the star instead of its movement during expansion and contraction.

The second equation of stellar structure is the equation of **hydrostatic equilibrium**. It describes the pressure profile $P(r)$ that must be established so that the buoyancy force balances gravity at every layer in the star.

$$\frac{dP}{dr} = -\rho \frac{GM_r}{r^2} \quad (3.2)$$

The third equation of stellar structure is the equation of **energy conservation**. It describes how the production rate of nuclear energy ϵ_{nuc} and gravitational energy ϵ_{grav} contributes to the luminosity, and takes into account the energy lost to neutrinos in ϵ_{ν} .

$$\frac{dL_r}{dM_r} = \epsilon_{\text{nuc}} + \epsilon_{\text{grav}} - \epsilon_{\nu} \quad (3.3)$$

The fourth and last equation of stellar structure is the equation of **radiative transfer**. It describes how the temperature profile $T(r)$ in the star is established through the transport of

energy by radiation.

$$\frac{dT}{dr} = -\frac{3\kappa\rho}{16\sigma T^3} \frac{L_r}{4\pi r^2} \quad (3.4)$$

Here, κ is the opacity of the gas which quantifies how much radiation is absorbed by the gas at a certain depth.

Finally, one must take into account an equation of state (EOS) $P(\rho, T, \mu)$, which couples the pressure with the density, temperature and mean molecular weight. Since there is no explicit dependence on a radial coordinate, this equation is not counted as an equation of stellar structure, but is no less important for a complete physical description of stars. Under normal conditions, the EOS takes the following form.

$$P = \frac{\rho k T}{\mu m_u} + \frac{4\sigma}{3c} T^4 \quad (3.5)$$

The first term describes the contribution of internal pressure for an ideal gas, the second term approximates radiation pressure for a black body.

Given an independent radial coordinate r , there are 5 unknown functions $M_r(r)$, $\rho(r)$, $P(r)$, $T(r)$, and $L_r(r)$. The opacity κ , the nuclear energy generation rate ϵ depend on density, temperature and chemical composition and can be extracted from data tables. We obtain a closed system of linear differential equations, which is complimented by a set of boundary conditions. On the surface, we postulate $r = R$, $\rho(R) = 0$, $P(R) = 0$, $L_r(R) = L$ and $M_r(R) = M$. The independent surface parameters L , R and M are finally reduced to only one by requiring that $M_r(0) = 0$ and $L_r(0) = 0$. We choose this free parameter to be the stellar mass M , whereas L and R must be found as part of the solution of the equations and their boundary conditions.

An analytic solution to the equations does not generally exist, which is why they can only be approximated numerically within a certain tolerance. The algorithm that is commonly used to achieve this is known as the *Henye method* (Henyey *et al.*, 1959; 1964), which is at the heart of many stellar evolution codes today.

3.1.2 Drivers of evolution

The stellar structure equations describe a star in hydrostatic equilibrium since we do not account for the dynamic transport of mass as would be observed for example in a collapse. In a typical numerical treatment, we consider that the star evolves *quasistatically*, i.e. the star is in hydrostatic equilibrium at all times and evolves on timescales that are much longer than the dynamical timescale. In practice, the evolution is computed in discrete timesteps, after each of which small changes are applied to the star and a new solution is found using the above equations.

There are multiple mechanisms that drive the evolution in stellar models. Most importantly, nuclear reactions take place in the central regions of the star, which change its chemical composition. This modifies the system of equations via the mean molecular weight μ , the opacity κ , and the nuclear burning rate ϵ_{nuc} . The star may also be chemically restructured by convective mixing, which takes place if there is a sufficiently high temperature gradient. In stellar evolution codes, convection is modeled using a form of mixing-length theory developed by Böhm-Vitense (1960), which defines a criterion for convection and a way of calculating the convective flux that can be applied to one-dimensional models. The chemical structure within a convective zone is assumed to be homogenized *instantly*.

Finally, all stars lose mass from their surface due to radiation pressure from the interior, which can have drastic effects on stellar structure and evolution. Since this is the focus of this work, I shall now describe in more detail the treatment of mass loss in stellar evolution codes.

3.2 Mass loss prescriptions

3.2.1 General remarks

As of today, there is no way to compute the mass loss of stars from first principles, owing to the enormous complexity of the physics involved and limited computational power. Therefore, stellar evolution models use prescriptions in order to compute the mass loss rate from simple stellar parameters. These prescriptions can originate from observations, theoretical calculations, or separate hydrodynamical stellar atmosphere models, and many different prescriptions have been proposed from each of these perspectives.

The mechanisms for mass loss differ depending on the evolutionary phase of the stellar surface. For example, mass loss of red supergiants is thought to be driven by infrared radiation interacting with dust and molecular gas at the stellar surface (Beasor & Davies, 2018), whereas winds of hot stars are predominantly induced by metallic absorption lines in the ultraviolet (Vink, 2022). As a result, different prescriptions are used for different phases of stellar evolution.

In this project, I focus on studying the effects of mass loss during the main sequence of massive stars, where they appear as hot O/B-type stars. I shall then compare this with the effect of post-main-sequence mass loss on stellar evolution. For this goal, I shall compute stellar models using three O/B mass loss prescriptions and two RSG mass loss prescriptions, which I describe in the following.

3.2.2 Mass loss of O/B-type stars

The current standard

The most commonly used prescription for O/B mass loss in stellar evolution codes is the one obtained by Vink *et al.* (2001) (hereinafter referred to as Vin01) from numerical wind models. This prescription gives separate equations for the mass loss rate in different temperature domains corresponding to the ionization states of iron (one of the dominant drivers of mass loss in hot stars). When the temperature cools across certain thresholds, the recombination of iron causes a change in the absorption line structure which results in a discontinuous increase in mass loss, known as a *bistability jump*. In this model, the first bistability jump (FeIV/FeIII) is located at around 25 000 K, and the second one (FeIII/FeII) at around 15 000 K, with the mass loss rate increasing by up to one order of magnitude across each of these jumps.

It is not clear whether the bistability jumps really exist or whether they are just artefacts of these specific wind models. An observational study by Crowther *et al.* (2006) found no discontinuities in the mass loss rate across temperature domains, and the new wind models by Björklund *et al.* (2022) also do not replicate this jump. Furthermore, late (cooler) O-type stars have been observed to have significantly weaker mass loss than predicted by Vin01, a discrepancy that has been referred to as the *weak wind problem* (Martins *et al.*, 2005; Puls *et al.*, 2008). These inconsistencies that have arisen over the past two decades motivate the study and implementation of more recent mass loss prescriptions for O/B stars.

In this study, I use the Vin01 \dot{M}_{OB} prescription as already implemented in the Geneva stellar evolution code (GENEC) and used in published grids of stellar models (e.g. Ekström *et al.*, 2012), applying it to stars with an effective temperature of more than $\log(T_{\text{eff}}) > 3.9$ and a surface hydrogen content of more than 30%.¹

¹For the sake of brevity, I shall not present the exact equations for this prescription here.

A new theoretical model

One of the most influential theories of stellar mass loss was established by [Castor *et al.* \(1975\)](#) and is commonly referred to as CAK theory after its three authors. The idea of this theory is to express the mass loss rate as a function of the Eddington parameter Γ_{Edd} which is defined as the ratio between the outward radiative acceleration and the inward gravitational acceleration on the surface and can be written as a function of stellar parameters as follows:

$$\Gamma_{\text{Edd}} = \frac{L\kappa}{4\pi GMc}, \quad (3.6)$$

with luminosity L , opacity κ , and stellar mass M . In order to simplify matters, κ is taken to be only the electron-scattering opacity, with the contribution of absorption lines being introduced into CAK theory via additional parameters known as *force-multipliers*. The mass loss rate is then calculated as a function of those force-multipliers, the stellar mass and the (electron scattering) Eddington parameter.

Recently, [Bestenlehner \(2020\)](#) (hereinafter referred to as [Bes20](#)) succeeded in removing the explicit dependence on stellar mass that remained present in the CAK mass loss rate, and proposed the following equation.

$$\log \dot{M}_{\text{OB}} = \log \dot{M}_0 + \left(\frac{1}{\alpha} + 0.5\right) \log(\Gamma_{\text{Edd}}) - \left(\frac{1}{\alpha} + 1\right) \log(1 - \Gamma_{\text{Edd}}), \quad (3.7)$$

where α is one of the aforementioned force-multiplier parameters, and \dot{M}_0 is a base mass loss rate that must be calibrated to external data. One of the characteristics of this mass loss theory is the presence of two different mass loss domains depending on which Γ -dependent term dominates. For small Γ_{Edd} , we have $\dot{M} \sim \Gamma_{\text{Edd}}^{1/\alpha+0.5}$, and for larger Γ_{Edd} (approaching unity), we have $\dot{M} \sim (1 - \Gamma_{\text{Edd}})^{-1/\alpha-1}$. Both Γ -dependent terms are equal at the transition value $\Gamma_{\text{Edd,trans.}}$, which is a function of α .

I implemented the version of this equation as calibrated onto observations of the Large Magellanic Cloud (LMC) by [Brands *et al.* \(2022\)](#), where $\log \dot{M}_0 = -5.19$ and $\alpha = 0.456$. Following the various assumptions of the model described in more detail in [Bestenlehner \(2020\)](#), I apply this prescription on stars with an effective temperature of above 30 000 K and surface hydrogen mass fraction of above 10^{-5} .

A new numerical model

New dynamically-consistent wind models were computed by [Björklund *et al.* \(2022\)](#), hereinafter referred to as [Bjo22](#). A grid of models across various stellar parameters was set up and a new equation for the mass loss rate was obtained by fitting to the model data.

$$\begin{aligned} \log \dot{M}_{\text{OB}} = & -5.52 + 2.39 \log \left(\frac{L}{10^6 L_{\odot}} \right) - 1.48 \log \left(\frac{M(1 - \Gamma_{\text{Edd}})}{45 M_{\odot}} \right) \\ & + 2.12 \log \left(\frac{T_{\text{eff}}}{45\,000 \text{ K}} \right) + \left(0.75 - 1.87 \log \left(\frac{T_{\text{eff}}}{45\,000 \text{ K}} \right) \right) \log \left(\frac{Z}{Z_{\odot}} \right), \end{aligned} \quad (3.8)$$

with luminosity L , stellar mass M , Eddington parameter Γ_{Edd} , effective temperature T_{eff} and metallicity Z . I implemented this mass loss rate for stars that fall into the parameter space explored by these wind models, given by $4.5 \leq \log(L/L_{\odot}) \leq 6.0$, $15 \leq M/M_{\odot} \leq 80$, $15\,000 \text{ K} \leq T_{\text{eff}} \leq 50\,000 \text{ K}$, and $0.2 \leq Z/Z_{\odot} \leq 1.0$.

3.2.3 Mass loss of red supergiants

In GENE models, a star is defined as a red supergiant if $\log(L/L_\odot) > 4$ and $\log(T_{\text{eff}}) < 3.7$. By default, the code uses a fit based on figures in [Crowther \(2001\)](#) with observational data from [Sylvester et al. \(1998\)](#) and [van Loon et al. \(1999\)](#) to compute the mass loss rate in this phase. The resulting prescription is given by the following equation, to which I will refer as [Cro01](#).

$$\log\left(\frac{\dot{M}_{\text{RSG}}}{M_\odot \text{ yr}^{-1}}\right) = -13.83 + 1.7 \log\left(\frac{L}{L_\odot}\right) \quad (3.9)$$

However, a large scatter of RSG mass loss rates has been observed for stars of similar luminosity, suggesting that other stellar parameters may play a role in determining RSG mass loss ([Beasor & Davies, 2016](#)). The correlation between mass loss rate and luminosity seems to be much tighter when considering only stars of a similar initial mass ([Beasor & Davies, 2016; 2018](#)). Based on this result, [Beasor et al. \(2020\)](#) conduct new observations using infrared photometry on globular clusters and propose the following prescription, to which I will refer as [Bea20](#).

$$\log\left(\frac{\dot{M}_{\text{RSG}}}{M_\odot \text{ yr}^{-1}}\right) = -26.4 - 0.3 \log\left(\frac{M_{\text{ini}}}{M_\odot}\right) + 4.8 \log\left(\frac{L}{L_\odot}\right) \quad (3.10)$$

I compared the effect of these two RSG mass loss prescriptions on the evolution of massive stars in detail as part of a previous “APL” semester project². In this work, the primary focus lies on the \dot{M}_{OB} prescriptions.

3.2.4 Other mass loss domains

In the previous subsections, I have presented the three \dot{M}_{OB} prescriptions ([Vin01](#), [Bes20](#), [Bjo22](#)) and the two \dot{M}_{RSG} prescriptions ([Cro01](#), [Bea20](#)) I will investigate. I have also introduced the *validity domain* of each of the prescriptions, which defines the range of stellar parameters where the prescription can be applied. However, mass loss is a ubiquitous process in stellar evolution and some prescription should therefore be active at all times during the evolution. Let us therefore briefly discuss the prescriptions used by GENE outside the domains of the O/B and RSG prescriptions.

Noteably, stars enter the theoretical Wolf-Rayet domain when the surface hydrogen abundance X_s drops below 0.3 at an effective temperature of more than 10 000 K, after which we apply characteristically high WR mass loss rates. Note that this treatment reverses the real chain of causality, since high mass loss is actually the origin – not the consequence – of WR-type classification, a problem we will discuss in depth later within this work. For now, we use the standard GENE implementation of WR type mass loss, which is to compute the WR mass loss rate according to [Nugis & Lamers \(2000\)](#), or [Gräfener & Hamann \(2008\)](#) when this prescription is valid. When using the [Bes20](#) prescription for O/B stars, I only switch to the WR prescriptions at a surface hydrogen threshold of 10^{-5} (instead of 0.3), as this prescription can supposedly also be used for hydrogen-containing WR stars.

Finally, for all domains not covered by one of the OB, RSG, or WR prescriptions, I use a common default provided by [de Jager et al. \(1988\)](#) (hereinafter referred to as [DJ88](#)), who gives the mass loss rate as long sums of Chebyshev polynomials of effective temperature and luminosity. The most significant gap in stellar evolution that is not covered by any other prescription is the yellow supergiant phase, where the star is cooler than required for the O/B prescriptions but too hot to

²Report here: <https://jorisjosiek.com/assets/documents/RSG-Mass-Loss-Report.pdf>

fall into the domain of the RSG prescriptions. In our models, [DJ88](#) can therefore be considered as a de facto YSG mass loss prescription.

3.3 The Geneva stellar evolution code

As previously mentioned, I shall compute stellar models using the Geneva stellar evolution code (GENEC; [Eggenberger et al., 2008](#)), an algorithm capable of simulating the evolution of stars from the ZAMS given some initial parameters such as mass, chemical composition and rotation rate. The code works by dividing the star into about 1000 discrete layers and then computing the hydrostatic solution of the (discretized) stellar structure equations using the Henyey algorithm. When this is done, the code evolves the star by a small timestep and applies changes to the physical structure according to mass loss rate prescriptions, nuclear burning networks, et cetera. Then the cycle repeats until a user-defined stopping point is reached (usually around $\sim 4\,000$ timesteps for the main sequence, and 25 000–45 000 timesteps for helium and carbon burning).

Because the code is designed to find hydrostatic equilibrium after each timestep, there is a possibility that convergence fails and no solution is found. This is more likely if the changes made during one timestep are very large (for example because of very high mass loss), bringing the star far away from equilibrium. GENEC has mechanisms to help models to converge in difficult situations. Firstly, the code possesses the ability to discretize space and time adaptively, automatically dividing the star into finer layers where needed and shortening the timesteps in order to make the evolution smoother. Secondly, the code includes the possibility for the user to change various parameters related to the numerical behavior of the algorithm, for example loosening convergence criteria. Inevitably, better convergence security and precision always comes at the cost of more computation time, as well as precious human time in case an intervention is needed.

In order to launch an evolution model with GENEC, one must first define the initial base parameters of stellar mass, rotation rate and metallicity. A tool provided with GENEC then generates an initial stellar model that is very close to the ZAMS. The star is initially chemically homogeneous, and at solar metallicity it is composed of 72% hydrogen, 26.6% helium and 1.4% metals distributed according to [Asplund et al. \(2005\)](#). A parameter file is created where the user can change additional parameters, for example choosing non-default mass loss prescriptions. Once GENEC is launched, the terminal output lets the user keep track of the general status of the computation, while the new stellar structure is regularly saved to the hard-disk (every 10 timesteps by default). In case of an interruption that cannot be resolved automatically, the code stops running but can be resumed from the last saved model after modifying some convergence parameters. At the end of the computation, we obtain a series of files containing data that describes the full stellar structure across its evolution. In order to avoid loading all of these files during post-processing, the global parameters of the star (e.g. luminosity, effective temperature, etc.) are condensed into a single file covering the entire evolution. Removing all unnecessary duplicates and log files generated during the computation, each model produces around 3–5 GB of data.

In order to analyze the data, I use a tool called `GENEC_toolBox`, a Python module containing an extraction and reduction pipeline designed to work with GENEC data. In addition to making all the evolution and structure variables available in the form of Python arrays, it can also generate a variety of predefined diagrams, with which the user can interact in order to investigate the models. Most of the analysis in this project was done in this way in Python, making extensive use of the libraries `numpy` ([Harris et al., 2020](#)) and `scipy` ([Virtanen et al., 2020](#)), as well as `matplotlib` ([Hunter, 2007](#)) to generate the graphics.

O/B- \dot{M}	RSG- \dot{M}	$M_{\text{ini}} [M_{\odot}]$
Bes20	Cro01	20, 25, 30, 40 [†]
	Bea20	20, 25, 30, 40
	—	50, 60, 66, 73, 80, 85, 95, 105, 120
Bjo22	Cro01	20, 25, 30, 40 [†]
	Bea20	20, 25, 30, 40
	—	50, 60, 66, 73, 80, 85, 120
Vin01	Cro01	20, 25 [†] , 30, 40 [†]
	Bea20	20, 25, 30, 40
	—	50, 60, 66, 73, 80, 85, 95, 105, 120

Table 3.1: Summary of the models computed with GENEC for the present study. Models marked with (†) did not complete central carbon burning.

3.4 Definition of the model grid

In this work, I have chosen to study stars of solar metallicity ($Z = 0.014$), a somewhat arbitrary choice as other metallicities are certainly also interesting to investigate. Furthermore, all of my models are of non-rotating stars, since rotation would introduce new effects that may override any conclusions relating simply to mass loss. Although I am computing models for only one metallicity and without rotation in order to constrain the parameter space, some possible effects of metallicity and rotation on the results will be discussed.

At several initial masses, which will be defined below, I compute a model using each one of the O/B mass loss prescriptions presented in [subsection 3.2.2](#), and for the models that reach the RSG phase ($M_{\text{ini}} \leq 40 M_{\odot}$), I compute two separate tracks using each one of the RSG mass loss prescriptions presented in [subsection 3.2.3](#).

When defining a model grid, it is customary to choose initial masses such that the ZAMS models are distributed approximately homogeneously in $\log L$. Published GENEC grids of massive stars present models with initial masses 20, 25, 32, 40, 60, 85 and 120 M_{\odot} ([Eggenberger et al., 2021](#); [Ekström et al., 2012](#); [Georgy et al., 2013](#)). In this work, I have used this grid as a starting point, but replaced the 32 M_{\odot} models with 30 M_{\odot} ones due to convergence issues, and included additional initial masses of 50, 66, 73, and 80 M_{\odot} with all O/B prescriptions as well as 95 and 105 M_{\odot} with [Bes20](#) and [Vin01](#) for a finer grid in the higher mass range. I chose the additional masses so that they remain approximately evenly distributed along $\log L$ above 40 M_{\odot} .

Finally, each model is computed from the ZAMS until the end of central carbon burning, defined as the point at which the central carbon mass fraction drops below 10^{-5} . The subsequent burning phases cumulatively last less than a year, accounting for roughly 0.00001 % of a massive star’s lifetime, while being comparatively arduous to compute. Since the change in surface parameters is negligible on this short timescale, and the likelihood of observing a star in these advanced phases is extremely slim, we have nothing to lose by excluding them from the computation.

For a complete summary of all 49 computed models, see [Table 3.1](#). Four models did not run until the end of central carbon burning due to convergence issues, but all models have at least reached the end of central helium burning. Where appropriate, incomplete models will still be included in the analysis.

CHAPTER 4

PREDICTIONS OF THE MODELS

4.1 Characterization of the mass loss prescriptions

4.1.1 *Validity timescales*

When I introduced the different \dot{M}_{OB} prescriptions in [Chapter 3](#), I also discussed their validity domains, which are based on a set of stellar parameters. In order to draw significant conclusions from the models regarding the impact of the prescriptions, we need to verify that they are indeed valid for a significant majority of the main sequence in the computed models. As a reminder to the reader, our models resort to the general mass loss rate given by [de Jager et al. \(1988\)](#) as a default if the chosen \dot{M}_{OB} prescription is not valid. However, this prescription is not the one we want to investigate for hot stars.

[Figure 4.1](#) shows the fraction of the MS that the models spend within their \dot{M}_{OB} prescription's respective domain of validity. The models show that [Vin01](#) is systematically valid for the complete MS, with the exception of the $120 M_{\odot}$ model, which actually switches to the WR mass loss rate (at $X_s < 0.3$) while still on the MS. Models using [Bes20](#) spend around 80–90% of the MS within this prescription's validity domain (i.e. $T_{\text{eff}} > 30\,000$ K) and exit it during MS cooling. The validity time fraction for [Bes20](#) peaks at $50 M_{\odot}$; it decreases for lower masses since the stars are already cooler at the ZAMS and thus closer to the edge of the validity domain. At higher masses, stars are hotter at the ZAMS, but also cool faster due to higher mass loss which increases the core-to-envelope mass ratio leading to faster expansion of the envelope. Models using [Bjo22](#) of at most $60 M_{\odot}$ spend all of the MS in their validity domain. However, the time fraction spent in the validity domain drops dramatically for higher masses due to the scope of the [Bjo22](#) wind model grids. For this reason, I will discard the 73, 80, 85, $120 M_{\odot}$ models of this prescription from further consideration. It is incidentally also the reason I did not compute additional high-mass models for [Bjo22](#).

4.1.2 *Average mass loss rate*

The mass loss rates are given in different forms by each of the prescriptions and depend on different parameters, making them difficult to compare directly. I therefore now present the average mass loss rate calculated by the prescriptions during their domain of validity.

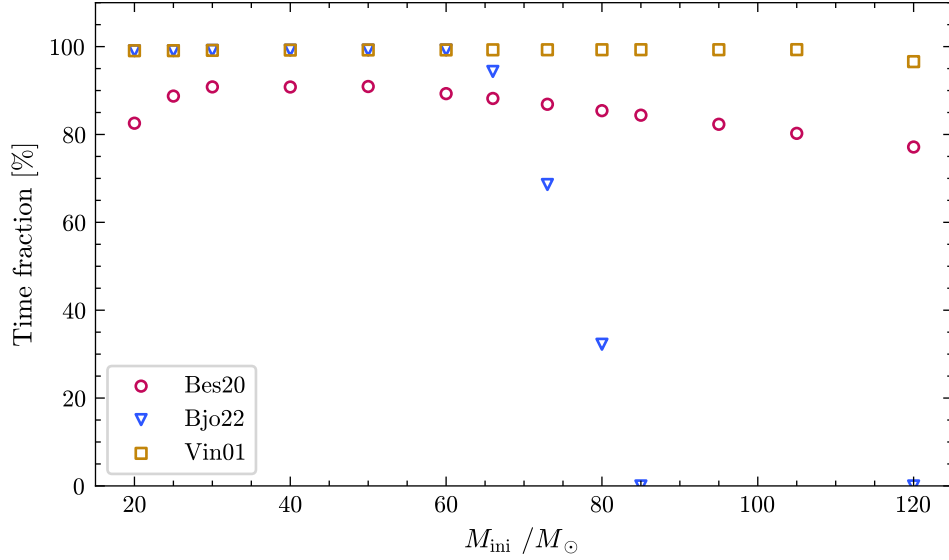


Figure 4.1: Time fraction of the main sequence spent within the validity domain of the chosen \dot{M}_{OB} prescription.

Using the model data, I specifically compute the time-averaged logarithmic mass loss rate¹ using the following equation,

$$\langle \log \dot{M} \rangle = \frac{\sum (\log \dot{M}_i)(t_{i+1} - t_i)}{\sum (t_{i+1} - t_i)}, \quad (4.1)$$

where the sum is over all timesteps i for which the mass loss rate is calculated according to the chosen prescription. For the O/B prescriptions, I additionally limit the sum to the main sequence, which makes the comparison between the mass loss rates more sensible, because some models re-enter their O/B mass loss prescription’s validity domain in the post-MS, which could skew the resulting average.

In addition to the average mass loss rate, I also compute error bars as the square root of the mean variance, as follows:

$$\delta(\log \dot{M}) = \sqrt{\frac{\sum (\log \dot{M}_i - \langle \log \dot{M} \rangle)^2 (t_{i+1} - t_i)}{\sum (t_{i+1} - t_i)}}. \quad (4.2)$$

The results are presented in [Figure 4.2](#) for \dot{M}_{OB} , and in [Figure 4.3](#) for \dot{M}_{RSG} . The errorbars are omitted for \dot{M}_{RSG} since they are all on the order of 0.05 dex and thus too small to be seen.

¹You may wonder why I am averaging the logarithmic mass loss rate instead of computing the logarithm of the average mass loss rate, i.e. why $\langle \log \dot{M} \rangle$ and not $\log \langle \dot{M} \rangle$? The answer is: in order to obtain a fuller picture of mass loss throughout the main sequence, it is important to consider that mass loss is a quantity typically given in orders of magnitude. If I computed the average of the absolute mass loss rate, the result would weigh strongly in favor of phases of strong mass loss, neglecting phases where mass loss may be orders of magnitude weaker, which are however just as important for a full characterization of a mass loss prescription.

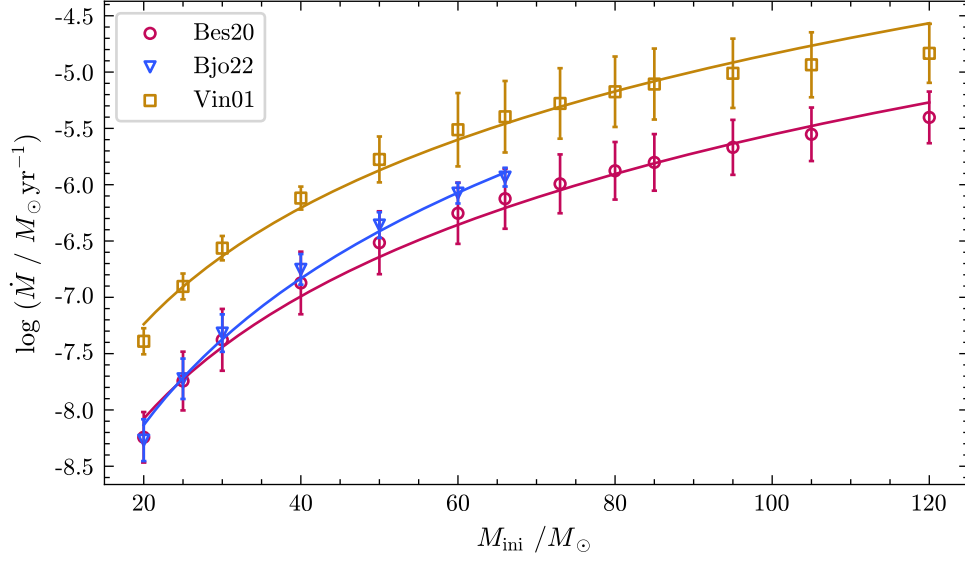


Figure 4.2: Time-averaged logarithm of the mass loss rate as a function of initial mass for the three O/B mass loss prescriptions, with power-law fits.

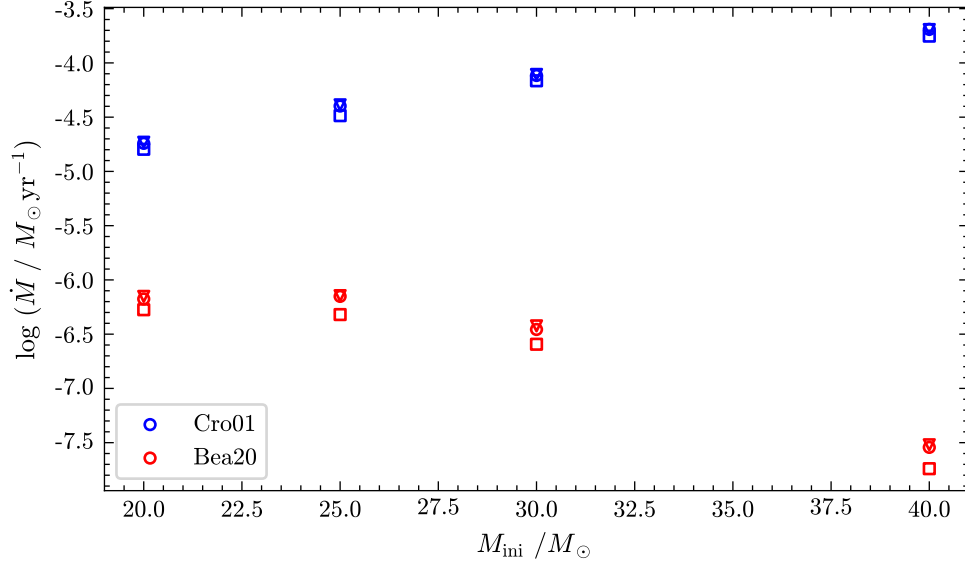


Figure 4.3: Time-averaged logarithm of the mass loss rate as a function of initial mass for the two RSG mass loss prescriptions. The shapes of the data points correspond the \dot{M}_{OB} prescription as in Figure 4.2.

\dot{M}_{OB} prescr.	a	b
Bes20	-8.08 ± 0.06	3.61 ± 0.11
Bjo22	-8.13 ± 0.06	4.33 ± 0.15
Vin01	-7.24 ± 0.05	3.43 ± 0.14

Table 4.1: Best fit parameters for the power law relating average mass loss during the main sequence to the initial mass. Parameter a represents the characteristic $\log \dot{M}$ of a $20 M_{\odot}$ star, and b is the exponent of the relation.

O/B mass loss

For each \dot{M}_{OB} prescription, the (logarithmically) averaged mass loss rate scales with the initial mass according to a power law of the form,

$$\langle \log \dot{M} \rangle = a + b \log \left(\frac{M_{\text{ini}}}{20 M_{\odot}} \right), \quad (4.3)$$

whose best fit parameters a and b were determined with the `optimize.curvefit` routine of the `scipy` package in Python and are plotted with the data in Figure 4.2 as well as shown in Table 4.1. We see that Vin01 consistently produces the strongest mass loss during the MS, while Bes20 mass loss is approximately an order of magnitude lower. The mass loss by Bjo22 is approximately the same as Bes20 at the lowest mass, but increases more with increasing mass than Bes20, surpassing it by approximately 0.3 dex at $66 M_{\odot}$.

Finally, we notice that the error bars for the mass loss rate computed with Vin01 are significantly larger for stars of at least $60 M_{\odot}$ than for the lower-mass range. This is due to the bistability jumps included in this prescription, each of which causes a discontinuous increase in the mass loss rate by up to one order of magnitude during the MS when the stellar surface temperature crosses certain thresholds.

RSG mass loss

For the models that become RSGs, it is evident that Cro01 predicts a much higher mass loss rate than Bea20. The difference between the two mass loss rates is approximately 1.5 dex for the $20 M_{\odot}$ models, and increases to an extreme 4 dex for the $40 M_{\odot}$ models. At this initial mass, stars are at the upper limit of the theoretical mass range to form RSGs, and observations of them are rare. For example, the Bea20 relation of mass loss rate to initial mass is based on a fit on cluster observations in which the most massive RSGs were of $25 M_{\odot}$ initial mass (Beasor *et al.*, 2020). There is therefore no observational basis to extend this mass loss rate prescription to include stars as massive as $40 M_{\odot}$, and we can consider this a mere numerical experiment carried out to investigate the effect of two contrasting \dot{M}_{RSG} prescriptions.

While the choice of \dot{M}_{RSG} prescription clearly dominates the dispersion in the applied mass loss rate in the RSG phase, there is also a small but noticeable effect of the \dot{M}_{OB} prescription that was applied in the MS. Models using Vin01 have a consistently lower \dot{M}_{RSG} than the models using other \dot{M}_{OB} prescriptions. This is due to these models losing more mass during the main sequence, causing them to enter the RSG phase at a slightly lower luminosity, which is linked to a lower mass loss rate with both \dot{M}_{RSG} prescriptions.

\dot{M}_{OB} prescr.	a	b/M_{\odot}
Bes20 ($M \leq 66M_{\odot}$)	0.869 ± 0.014	3.1 ± 0.6
($M \geq 80M_{\odot}$)	0.601 ± 0.007	4.2 ± 0.7
Bjo22 ($M \leq 66M_{\odot}$)	0.898 ± 0.019	2.6 ± 0.8
Vin01 ($M \leq 50M_{\odot}$)	0.76 ± 0.04	5.3 ± 1.3
($M \geq 60M_{\odot}$)	0.458 ± 0.019	10.0 ± 1.7

Table 4.2: Best fit parameters of the linear fits relating the TAMS mass to the initial mass in the different mass loss regimes

4.2 Main sequence evolution

I now investigate in more detail the evolution of the models during the main sequence. Since models of the same mass begin at the ZAMS in exactly the same state, differences in their MS evolution are due solely to the different mass loss rates, making this phase the simplest to interpret. In addition, no dramatic structural changes take place in the MS, resulting in comparatively smooth evolutionary tracks free of numerical instability. Here, I will establish how MS mass loss sets the stage for a star’s late-phase evolution, which will enable a later discussion linking possible phenomena in evolved stars back to the main sequence.

4.2.1 Mass loss regimes

First we investigate the total mass lost during the main sequence. I define the end of the main sequence, or TAMS, as the moment where the central hydrogen mass fraction in the star drops below 10^{-5} . In [Figure 4.4](#) I then present the mass at the TAMS as a function of the initial (ZAMS) mass for all the models. It is clear that the models using [Vin01](#) and [Bes20](#) can be divided by initial mass into two distinct regimes in each of which the total mass lost during the MS follows a tight linear trend. We parametrize a simple linear fit according to

$$M_{\text{TAMS}} = aM_{\text{ini}} + b \quad (4.4)$$

and present the fitting parameters in [Table 4.2](#).

Since [Bjo22](#) does not span the entire mass range, we do not see two regimes for this prescription. Extrapolating it to higher masses would likely not reproduce the break observed for the other prescriptions, since both [Vin01](#) and [Bes20](#) directly imply the existence of two mass loss regimes, while [Bjo22](#) does not. [Vin01](#) makes a regime transition at around $\sim 50\text{--}60 M_{\odot}$ due to the bistability jump representing a switch in line opacity due to a change in the ionization balance of iron, which ultimately affects the mass loss rate. [Bes20](#) encodes two mass loss regimes in one equation, representing optically thin (weak) and optically thick (strong) winds. The characteristic variable here is the Eddington parameter Γ_{Edd} and its transition value $\Gamma_{\text{Edd,trans}} \approx 0.47$. In [Figure 4.5](#) we see the evolution of Γ_{Edd} for a selection of models using the [Bes20](#) \dot{M}_{OB} , showing that models with an initial mass of more than $\sim 66 M_{\odot}$ may reach the optically thick wind regime during their MS and thus significantly increase their mass loss. This explains the regime transition at around $\sim 70\text{--}80 M_{\odot}$ seen in [Figure 4.4](#) for this prescription.

It is noteworthy that although both [Bes20](#) and [Vin01](#) predict the existence of two mass loss regimes (which can ultimately be traced back to opacity changes in the atmosphere), the regime transition happens at different masses for either of these prescriptions. Additionally, the value

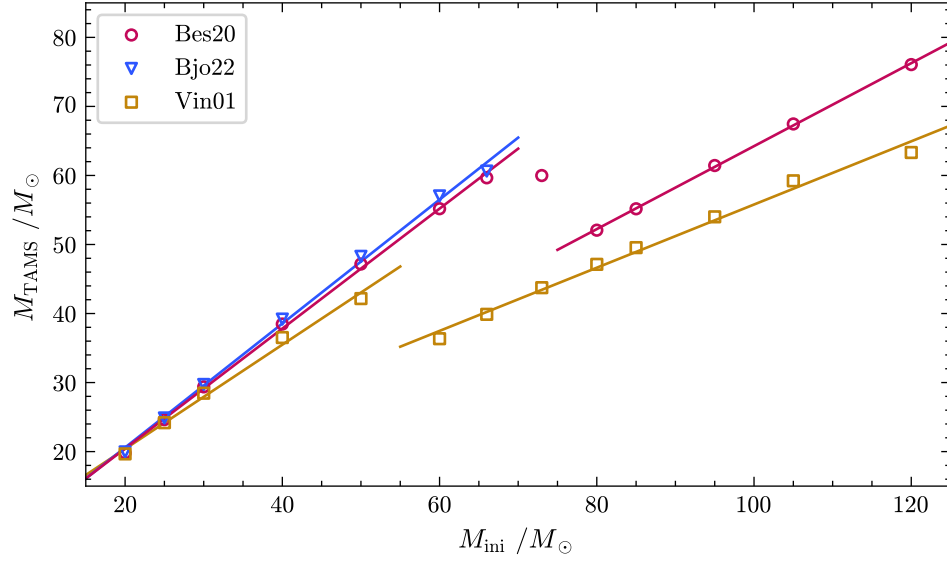


Figure 4.4: TAMS mass as a function of initial mass for the three \dot{M}_{OB} prescriptions, with regime-wise linear fits.

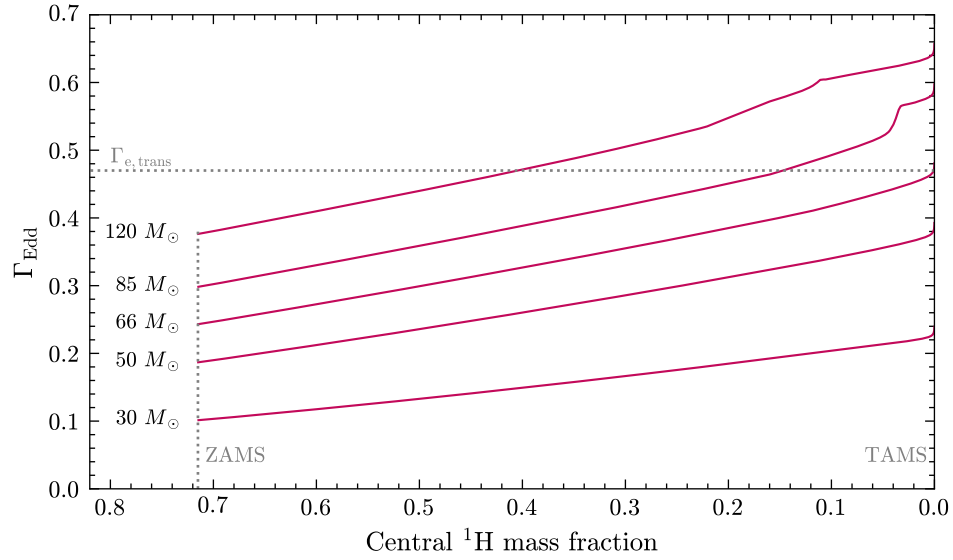


Figure 4.5: Main-sequence evolution of the Eddington parameter for selected models using the Bes20 \dot{M}_{OB} prescription. The horizontal dotted line marks the transition between the optically thin and optically thick wind regime.

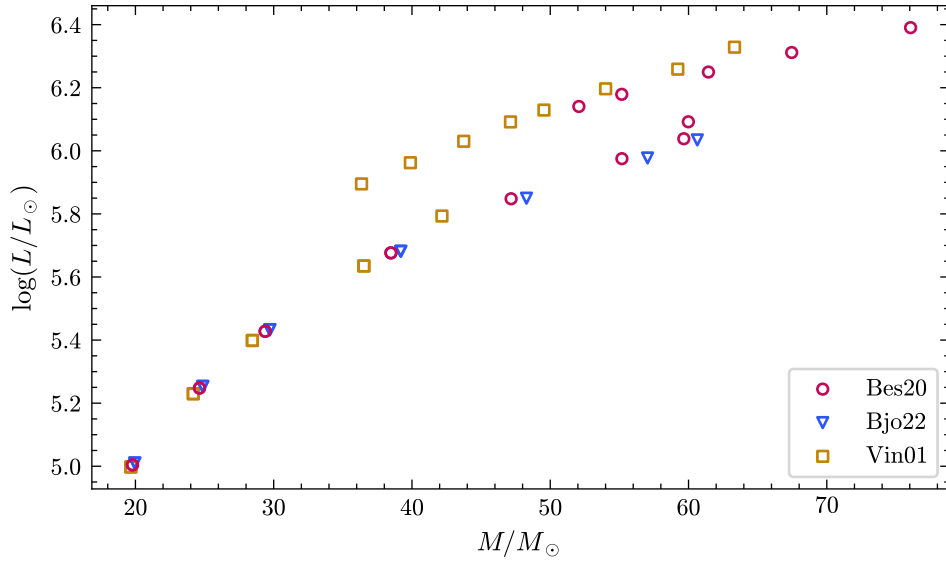


Figure 4.6: Mass-luminosity relation for the models at the TAMS

of $\Gamma_{\text{Edd,trans}}$, which directly determines the transition mass for [Bes20](#) (see [Figure 4.5](#)), does not depend on the scaling of the mass loss rate $\log \dot{M}_0$, but only on the force-multiplier α . However, it is not very sensitive to the value of α : for $\alpha = 0.2$ we would have $\Gamma_{\text{Edd,trans}} = 0.485$, and for values as high as $\alpha = 0.8$ we obtain $\Gamma_{\text{Edd,trans}} = 0.457$. Since α is expected to fall well inside the range 0.2–0.8 for a wide range of temperatures and metallicities (See [Puls et al., 2000](#), Table 3), we conclude that [Bes20](#) makes a solid prediction of the regime transition mass that depends very little on any other parameters.

A consequence of the two mass loss regimes is the establishment of a bimodal mass-luminosity relation by the end of the MS, as evident in [Figure 4.6](#). The upper sequence in this relation consists of models in the high mass loss regime. A higher mass loss rate during the MS does indeed slightly reduce the luminosity at the TAMS, as we will explore in the following section, but this decrease in luminosity does not compensate for the mass reduction enough for the model to stay on the same M – L relation. We may yet wonder what the structural difference is between the stars of each mode of the mass-luminosity relation. Let’s take for example two stars that both have a mass of $40 M_{\odot}$ at the TAMS. One of the stars has only a slightly higher initial mass and spent the MS in the low mass loss regime; the other had an initial mass of the order of $\sim 70 M_{\odot}$ and spent the MS in the high mass loss regime. The initially more massive star has lost more of its hydrogen-rich envelope and had a larger hydrogen-burning core while on the MS, which means it now has a higher helium content and therefore a higher mean molecular weight μ at the TAMS than its initially less massive counterpart. It is relatively straightforward to show that the luminosity L scales as μ^4 (see [Appendix B](#)), which explains the higher luminosity of the more helium-rich star at the TAMS.

4.2.2 Evolution in the Hertzsprung-Russell Diagram

The Hertzsprung-Russell diagram (HRD) is one of the most valuable visualization tools in stellar astrophysics. It is a two-dimensional plot that displays the luminosity of a star and its effective temperature, which are two of the most important surface parameters that play a fundamental role for mass loss, with most prescriptions being directly or indirectly related to at least one of these

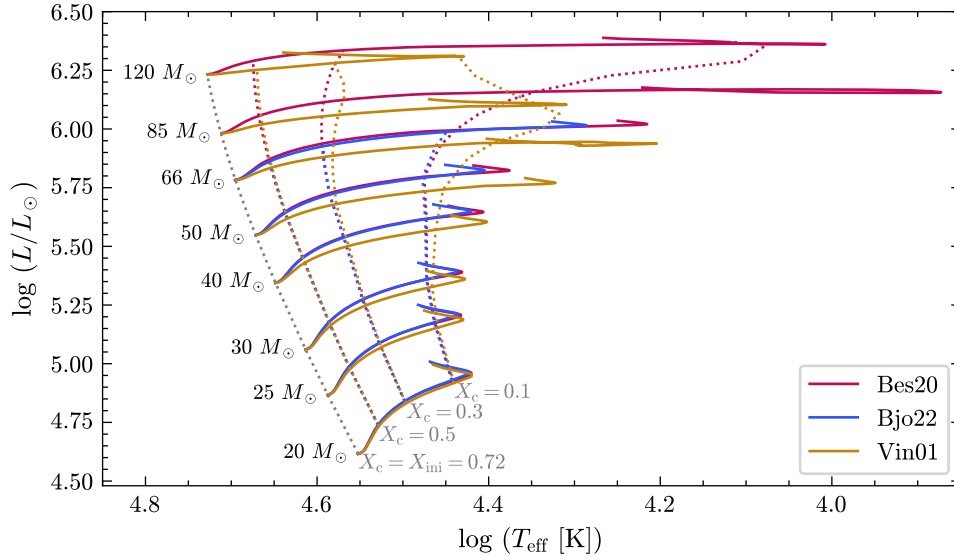


Figure 4.7: Hertzsprung-Russell diagram showing the evolutionary tracks of selected models during the main sequence. Additionally, dotted curves represent the location of the models at various central hydrogen mass fractions X_c as markers for evolutionary progress.

variables. Furthermore, the HRD implicitly displays a third variable, namely the stellar radius which is uniquely encoded by each point on the HRD through the Stefan-Boltzmann relation in Equation 2.1. The radius increases as one moves towards the top-right of the HRD ($T_{\text{eff}} \downarrow$, $L \uparrow$).

In stellar evolution modeling, it is common to represent the evolution of a star as a track on the HRD, and many phases of stellar evolution are associated with tracks of a characteristic shape. We will encounter this kind of diagram multiple times throughout this work, since it can be used as a starting point to understand precisely how the (observable) surface phenomena evolve and how they relate to the interior processes in a star.

In this section, I perform a detailed analysis of main sequence evolution in the HRD, while presenting some additional figures to highlight some important aspects. The MS tracks in the HRD are shown for some select models in Figure 4.7. In this diagram, I also show curves of equal central hydrogen mass fraction X_c in order to compare models at similar stages in their MS. The models begin on the ZAMS at $X_c = 0.72$, which traces a curve in the HRD on which the more massive stars are placed at the hotter, more luminous end.

During the MS, the stars begin to cool, as well as slightly increase their luminosity. For most of the MS, this evolution is rather gradual: indeed, we see only marginal change in the HRD until $X_c = 0.3$. The origin of this slow cooling expansion lies in the evolution of the convective core, which is shown on Figure 4.8. At the ZAMS, the ignition of hydrogen burning establishes a steep temperature gradient in the stellar interior which generates a large convective region encompassing 50–90 % of the total stellar mass. During the evolution, the mean molecular weight μ in the core increases due to nuclear fusion, which results in a drop in gas pressure according the ideal gas EOS, leading to a progressive contraction of the core. The core contraction induces a small boost of the nuclear reaction rates, increasing the luminosity, as well as the production of excess thermal energy which is transported outward. This has two effects: firstly, the temperature gradient is smoothened, leading to a reduction of the central convective region throughout the MS, as evident on Figure 4.8. Secondly, the envelope is slowly heated from below and expands while on the MS,

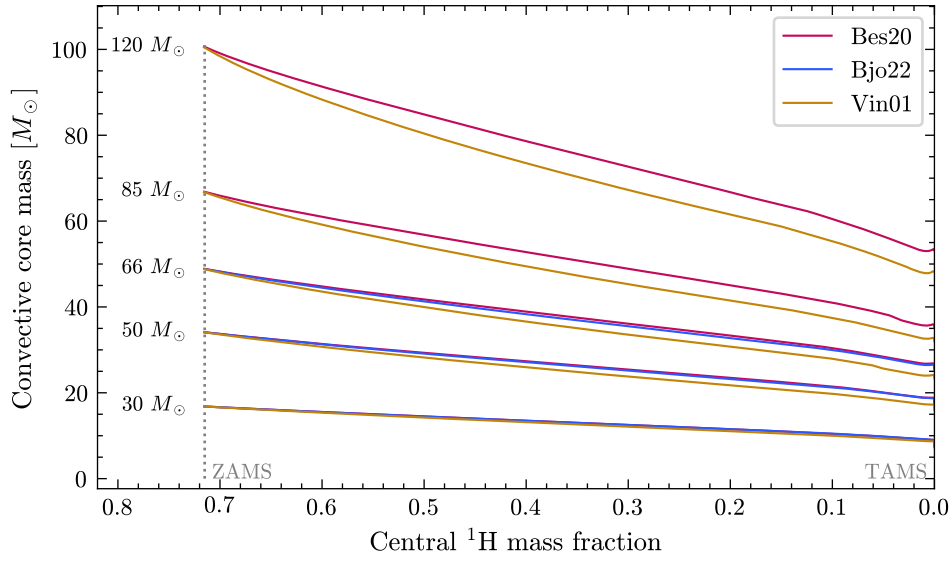


Figure 4.8: Main-sequence evolution of the convective core mass for selected models.

as is evident on the HRD.

When hydrogen in the core is almost depleted, the nuclear energy production rate begins to drop, which reduces radiation pressure in the star. This causes a brief phase of contraction at the very end of the main sequence, which manifests itself in the HRD by a short blueward “hook” at the end of the tracks.

At this point, it is worth briefly introducing the interior chemical evolution of stars on the MS, since this will play an larger role for the discussion of late-phase evolution. Figure 4.9 shows snapshots of the interior abundance profile of the $60 M_{\odot}$ model with Bes20 \dot{M}_{OB} at different points of the MS. We see that three distinct regions are established during the MS: (1) The convective core, which is chemically homogeneous and decreases in size throughout the MS; (2) The layers of gas that used to be part of the central convective region earlier in the evolution but whose chemical composition has been frozen in time at the moment they stopped being convective; and (3) the envelope consisting of layers that were never in contact with the core and therefore have the same chemical composition as the star on the ZAMS. The resulting chemical profile is one that is hydrogen-depleted in (1), hydrogen-rich in (3), with a transition region in (2). Furthermore, mass loss from the surface slowly removes material from the envelope (3), but indirectly affects the size of all three regions, as will be discussed in the following. The model chosen for Figure 4.9 is simply one example, and the evolution of other models with different mass loss prescriptions is qualitatively similar to the one shown here.

After having gained a detailed understanding of main sequence evolution of massive stars from the models, we now discuss how mass loss affects the processes involved. First, let us consider more closely the evolution of the effective temperature. Looking again at the HRD in Figure 4.7, we see that for lower masses, the effective temperature reaches its minimum at a relatively similar value of around $\log(T_{\text{eff}} [\text{K}]) = 4.3$, which then begins to visibly decrease above $\sim 50 M_{\odot}$. This happens mainly because of increasing mass loss making the envelope less massive, which makes it react more sensitively to the heat released from core contraction by expanding more. This explains why the Vin01 models up to $66 M_{\odot}$ reach lower effective temperatures than their counterparts with lower mass loss rates. At the highest masses, the mass loss is so high that a different effect

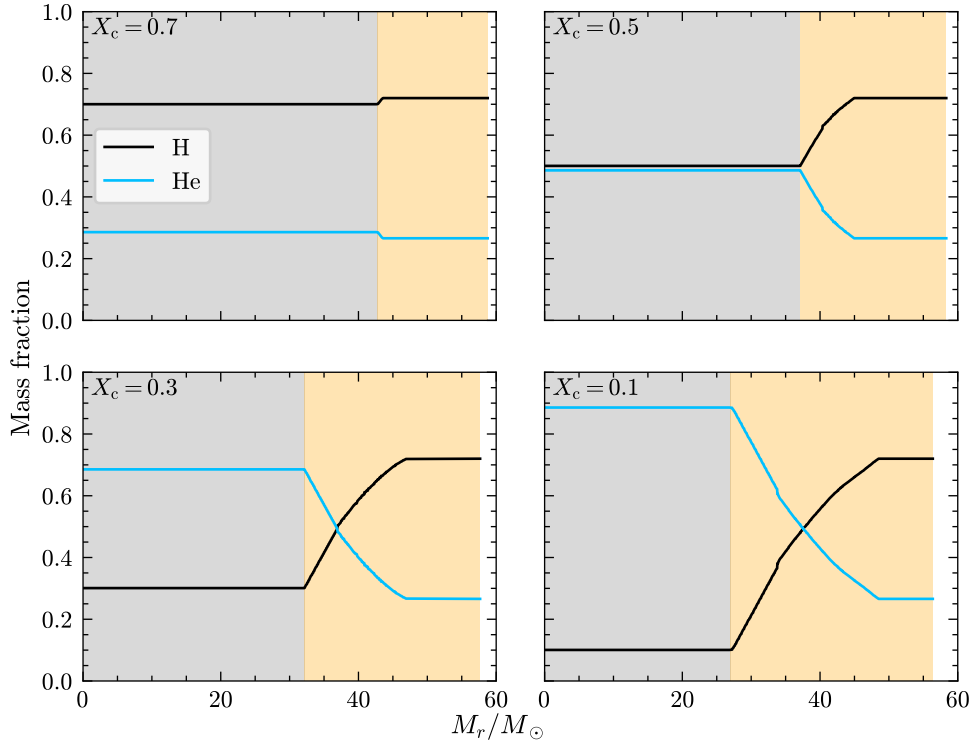


Figure 4.9: Snapshots of the abundance profile of the $60 M_{\odot}$ model with [Bes20](#) at different moments of the MS ($X_c = 0.7, 0.5, 0.3, 0.1$), showing the internal distribution of hydrogen and helium as a function of the radial mass coordinate. The shaded gray area shows the extent of the convective core, with the shaded yellow area representing the envelope.

begins to dominate, namely the exposure of layers considerably deeper and hotter in the stellar structure; thus the minimum effective temperature begins to increase again for the strong [Vin01](#) \dot{M}_{OB} at high masses, and to a lesser extent for the weaker [Bes20](#) \dot{M}_{OB} . Interestingly, the results show that some models using the [Bes20](#) \dot{M}_{OB} are able to become YSGs while still on the main sequence, owing to their mass loss being strong enough to ease the inflation of the envelope, but not too strong as to expose hotter layers.

Apart from the noticeably different temperature ranges of the models, we remark that the tracks using [Vin01](#) evolve at a slightly lower luminosity compared to the other \dot{M}_{OB} prescriptions due to the higher mass loss rate. This is because the star requires less radiation pressure support in hydrostatic equilibrium at a lower mass, which results in a more compact hydrogen-burning region in the core as well as a smaller central convective region. Importantly, the MS is sufficiently long that the stellar core has the time to adjust in this way to the mass lost from the surface. The result is that stars with a higher \dot{M}_{OB} produce less helium than stars with a lower \dot{M}_{OB} . Therefore, stellar winds can be viewed as a damper of nucleosynthesis not only by directly removing hydrogen from the star, but also by preventing additional hydrogen *within* the star from being converted to helium later. Conversely, stars with lower mass loss have larger central convective regions, allowing for more hydrogen to be pulled into the core. The more general conclusion to be stressed from this result is the following:

Mass loss during the main sequence has the ability to affect the interior structure of stars due to long timescales on which the interior processes can react to the mass loss.

This conclusion will be revisited more explicitly in the following subsection, where we will encounter some of its more dramatic examples.

4.2.3 Surface enrichment and interior feedback

Theoretical modeling allows us to have complete information about stellar interiors, which is mostly elusive to observers. However, heavy mass loss can eventually bring layers to the surface that were once obscured, which shows that understanding the evolution of stellar interiors could potentially help explain observable phenomena. I have already touched upon stellar interiors in the previous discussion about the convective core, and it is now time to consider the complex interplay between mass loss and interior structure more deeply. For this, I will for the first time extend the analysis beyond the main sequence in order to show the full scope of these effects, as well as transition into the study of more evolved stars.

It is an overly lengthy endeavor to study in detail the interior structure of all of the models as well as its evolution in time. Instead, I will focus on the evolution of the surface hydrogen abundance, since this is an useful tracer of the history of the interior stellar structure. In a manner of speaking, the hydrogen abundance measured at the surface layer is an archeological record of the processes experienced by that layer when it was still part of the stellar interior, before it was uncovered by mass loss. Furthermore, the surface hydrogen mass fraction is one of the defining parameters for WR stars, which will be the focus of discussion in the next section.

Consider [Figure 4.10](#), which shows the evolution of the surface hydrogen abundance for three different initial masses. The x -axis shows the total mass lost as a fraction of its initial mass as a proxy for evolution, which enables us to directly compare the models at the same mass. For future reference, let us refer to $X_s(\Delta M)$ plotted here as the *hydrogen depletion curve*² of a given stellar model. It is a function that relates surface hydrogen depletion directly to mass loss, while not being *explicitly* dependent on the mass loss rate. Importantly, the hydrogen depletion curve is not an abundance profile of the star at a fixed point in time, but an evolutionary curve!

The first, perhaps surprising conclusion from comparing the model results is simply the fact that they are different. This shows that there must be some feedback mechanism which lets mass loss impact the chemical structure of interior layers *before* they are brought to the surface. As we will see, the crucial link in this chain is convective mixing, being one of the most important drivers of chemical evolution in stars. We have already seen how mass loss can slightly alter the size of the convective core during the main sequence, and we will now explore further how mass loss affects the formation of convective regions during key evolutionary phases.

Before I analyze the results shown in [Figure 4.10](#) in detail, let us consider how to interpret various features in the hydrogen depletion curve in general. Specifically, we investigate the meaning of its gradient $\left| \frac{dX_s}{dM} \right|$ by classifying it into three qualitative cases.

- (1) The gradient is zero, i.e. the removal of mass from the surface does not significantly alter the hydrogen abundance. If there is a plateau in the hydrogen depletion curve over a certain mass range, we can conclude that this region was at some point chemically homogenized by the presence of convection before being brought to the surface. If any nucleosynthesis took place in this region, it happened before the convection stopped.
- (2) The gradient is very steep, i.e. the removal of some mass layer causes a sharp transition in the surface hydrogen abundance. This indicates the presence of a boundary between two

²I invented this term in order to make discussion a little more concise, so you won't find any references to it in the literature.

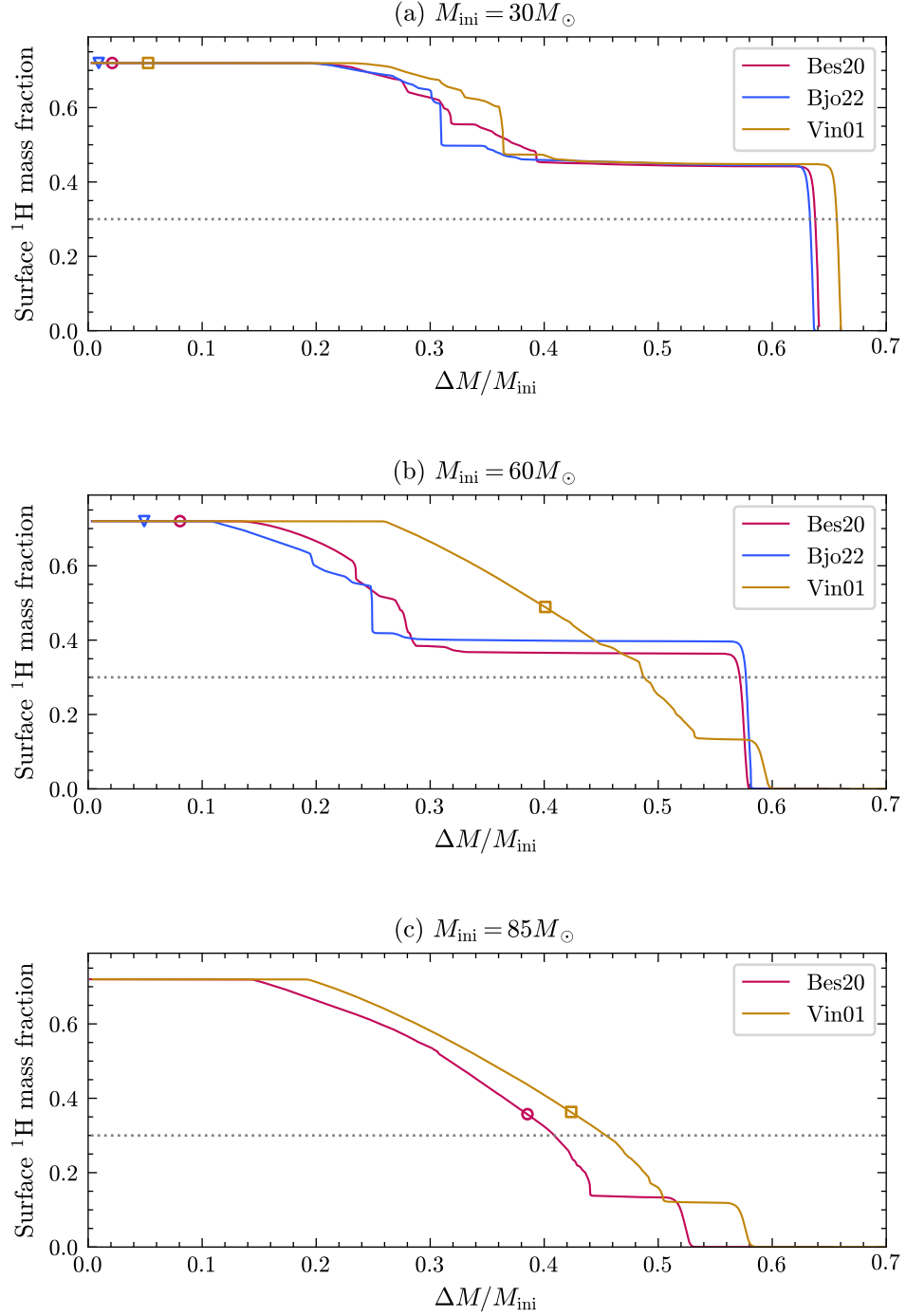


Figure 4.10: Evolution of surface hydrogen abundance as a function of relative mass lost for models with initial masses (a) $30 M_{\odot}$ (with $\text{Cro01 } M_{\text{RSG}}$), (b) $60 M_{\odot}$, (c) $85 M_{\odot}$. The horizontal dotted line shows the threshold of $X_s = 0.3$ as the definition of WR stars. The plotted shapes mark the location of the TAMS on each model.

chemically distinct regions, which is most likely the edge of a former convective zone.

- (3) The gradient is gradual, i.e. there is a steady decline in surface hydrogen abundance with mass loss. This pattern tends to appear when a shrinking convective zone hosts hydrogen burning at its base, so that material get deposited less high the more H-depleted it becomes.

As we can see, convection in the interior of stars leaves multiple signatures in the hydrogen depletion curves. It is important to note that these features are fossils of *former* convective zones which are no longer convective when they reach the surface. In general, massive stars never exhibit convective regions that extend all the way to the surface. It should also be mentioned that we could perform the same exercise with other elements such as helium or carbon, depending on which regions and phases we are interested in tracing.

Let us finally turn to the specifics of Figure 4.10. First, we remind ourselves that the only difference between the models shown on each plot is the mass loss rate applied during the main sequence. Thus, all the features found in the tracks, even after the main sequence, can be related back to a difference in the chosen \dot{M}_{OB} . Now let us focus on the $60 M_{\odot}$ models, since they exhibit contrasting mass loss with Bes20 and Bjo22 still in the low mass loss regime and Vin01 already in the high mass loss regime. The main consequence of being in the high mass loss regime is that the Vin01 model starts to be hydrogen-depleted while still on the MS. This happens when the layers that used to be in the convective core are revealed at the surface (case 3 in the above analysis).

After the main sequence is over and helium ignites in the core, hydrogen burning will typically move to a shell above the core. The ignition of the hydrogen-burning shell will induce the formation of a large convective zone spanning most of the envelope, which will quickly reduce to a slightly smaller size and remain there during most of hydrogen shell burning. The remnant of this convective region manifests itself as a plateau in the hydrogen depletion curves in Figure 4.10 (case 1). The width of this plateau (i.e. the size of the convective region) correlates with the mass of the envelope that lies above the hydrogen-burning shell at the moment of its ignition, which is a direct result of the total mass lost during the main sequence. Furthermore, a larger convective region can pull more hydrogen-rich material from the upper layers into the interior, resulting in wider plateaus on hydrogen depletion curves being generally more hydrogen rich than the narrower ones. At the end of the plateaus, the models reach the bottom boundary of the former convective region, where the layers rapidly becomes more hydrogen-poor as they near the center of hydrogen shell burning. After this limit, the hydrogen has been completely removed and star exposes its helium rich core³.

Still looking at the $60 M_{\odot}$ models, we notice that Bjo22 and Bes20 start to become hydrogen-depleted after less mass loss than Vin01. This is for two reasons. Firstly, the large convective region formed at shell hydrogen ignition dredges up H-poor material closer to the surface than the ZAMS core convective region. Secondly, there is also a small effect of diffusion, which is a form of chemical transport that acts on long timescales and in the absence of convection. Since these effects only become important after the MS, they only affect the models with Bjo22 and Bes20, but not Vin01.

In general, the hydrogen depletion curve can be characterized into the following zones (shown schematically in Figure 4.11): (I) constant hydrogen envelope, (II) gradual decline either from convective dredge-up (later) or by reaching the ZAMS convective core (earlier), (III) plateau representing the convective region of the hydrogen-burning shell, (IV) sharp drop of the hydrogen abundance to zero. In the high MS mass loss regime, the plateau (III) is hydrogen-poor and narrow, and in the low MS mass loss regime, it is hydrogen-rich and wide. This zone model will be relevant for the study of Wolf-Rayet evolution, since this is intrinsically linked to the evolution of surface hydrogen.

³This type of star is known as a *stripped star*.

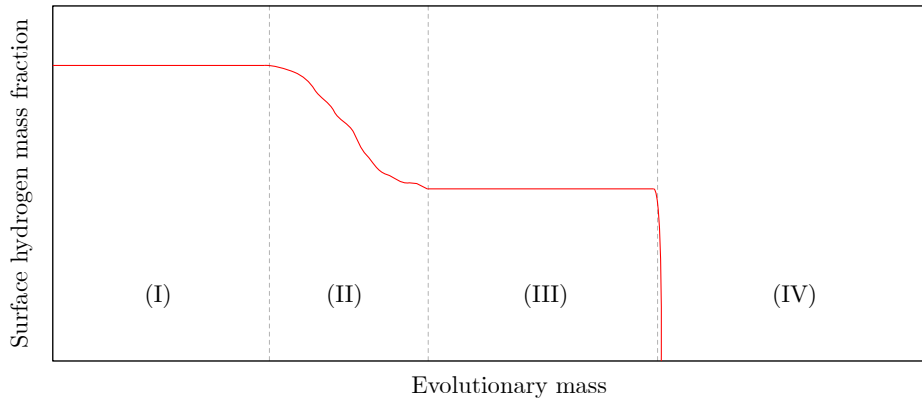


Figure 4.11: Schematic hydrogen depletion curve depicting the characteristic zones.

We conclude that the mass loss rate applied during the main sequence can have a large impact on the evolution of the interior chemical structure of the star, which may eventually show itself at the surface. This reinforces the point we first encountered in the previous section regarding the convective core, and shows that the effect of main sequence mass loss is not as straightforward as simply removing layers from the surface. In the later evolution, the nuclear timescale becomes much shorter than the mass loss time scale, which means that the stellar core evolves at a rate so fast that the change in stellar mass no longer plays any significant role. Finally, we should keep in mind that the present analysis is valid for single, non-rotating stars. The structure of convective zones may be much more complicated if we consider the impact of rotation, internal gravity waves or tidal forces.

Now, we will turn the focus away from the main sequence towards a special kind of evolved hydrogen-depleted star: the Wolf-Rayet star.

4.3 Formation and evolution of Wolf-Rayet stars

Before we begin to discuss the formation of WR stars in the models, let me first revisit their definition as well as provide some context on their importance in astronomy. We remind ourselves that the “Wolf-Rayet” type of star is defined as a spectral class characterized by strong and broad emission lines, which is an indicator of a strong optically thick wind that obscures the photosphere of the star (Abbott & Conti, 1987). Since WR stars are the last evolutionary phase of the most massive stars, their structure and evolution play a vital role in determining the ultimate nature of their supernova explosions. Indeed, most of the hydrogen-deficient type Ib/Ic SNe are commonly thought to have a hydrogen-poor WR-type progenitor (Dessart *et al.*, 2017; Groh *et al.*, 2013; Schweyer *et al.*, 2023). During the SN explosion of stars that have experienced high mass loss, the shock front can interact with the material previously ejected by winds (Dessart *et al.*, 2022), a phenomenon that has even been observed in rare cases (Gal-Yam *et al.*, 2014; Groh, 2014). Ejecta from stars (by winds and SNe) are a vital component of the baryonic cycle of galaxy evolution (Péroux & Howk, 2020), and they are the only source of metal-enriched material. Therefore, it is important to study the role of evolved stars as ejectors of winds as well as progenitors of supernovae.

In stellar evolution modeling, we do not obtain spectra of stars from which we could determine their spectral type. A correlation between spectral type and stellar parameters must therefore

Type	$\log(T_{\text{eff}} [\text{K}])$	X_s	
WNL	≥ 4	$10^{-5} - 0.3$	$C \leq N$
WNE			
WC	$4 - 5.25$	$\leq 10^{-5}$	$C > N$
WO	≥ 5.25		

Table 4.3: Evolutionary definition of WR subtypes.

be assumed in order to be able to put our models into a spectral class. These correlations have been established observationally and from stellar atmosphere models, however it is important to remember that they are not perfect fits. One must keep in mind that especially in exploratory studies such as this one, evolutionary calculations may yield exotic kinds of stars that may not fit in any observational class. In general, special care must be taken when comparing parameters obtained from models and from observations.

In our models, we define a star as WR when its effective temperature is above 10 000 K and its surface hydrogen abundance below 0.3. Typically, WR are further divided into subclasses based on the relative strength of carbon, nitrogen and oxygen spectral lines. Since spectral line strength is mainly determined by temperature and element abundances, we classify the WR stars subtypes using these criteria in Table 4.3. Note that these definitions differ slightly from the ones previously used in Geneva WR grids in Georgy *et al.* (2012), following a study of spectra generated from evolutionary models (Groh *et al.*, 2014).

4.3.1 Young WR stars

I shall present some parameters of the models at the moment they enter the WR phase according to evolutionary criteria. This will enable us to characterize freshly-formed WR stars. From the computations, all the models of at least $50 M_{\odot}$ reach the WR phase, as well as all the $30 M_{\odot}$ and $40 M_{\odot}$ models using the Cro01 \dot{M}_{RSG} and the $25 M_{\odot}$ using the Bjo22 \dot{M}_{OB} and the Cro01 \dot{M}_{RSG} . None of the models using the Bea20 \dot{M}_{RSG} become WR stars because the RSG mass loss is too weak.

Figure 4.12 shows a corner plot of various model parameters at the point of WR formation. It includes scatter plots displaying the relations between initial mass M_{ini} , evolutionary mass M , Eddington parameter Γ_{Edd} , luminosity L , time t scaled by the MS timescale τ_{MS} , and effective temperature T_{eff} . We shall now discuss some interesting properties of these results by focusing on some of the individual panels.

Mass (M) – Initial mass (M_{ini})

The results show a tight correlation between mass and initial mass that seems to be only marginally affected by the chosen mass loss rate. Compared to the large mass dispersion on the TAMS (Figure 4.4), the mass at the beginning of the WR phase seems to be very predictable regardless of mass loss rate. Merely in the range of $80\text{--}95 M_{\odot}$ do we notice the weaker Bes20 \dot{M}_{OB} leading to WR formation at a higher mass than the Vin01 models by up to $5 M_{\odot}$. This is due to a larger convective core in the Bes20 models leading to faster hydrogen depletion, as explored in the previous sections. However, given those conclusions regarding the hydrogen depletion curve, we could expect the mass dispersion here to be much more dramatic. Indeed, the results I had presented for the $60 M_{\odot}$ models in Figure 4.10 suggest that the Vin01 model should become WR

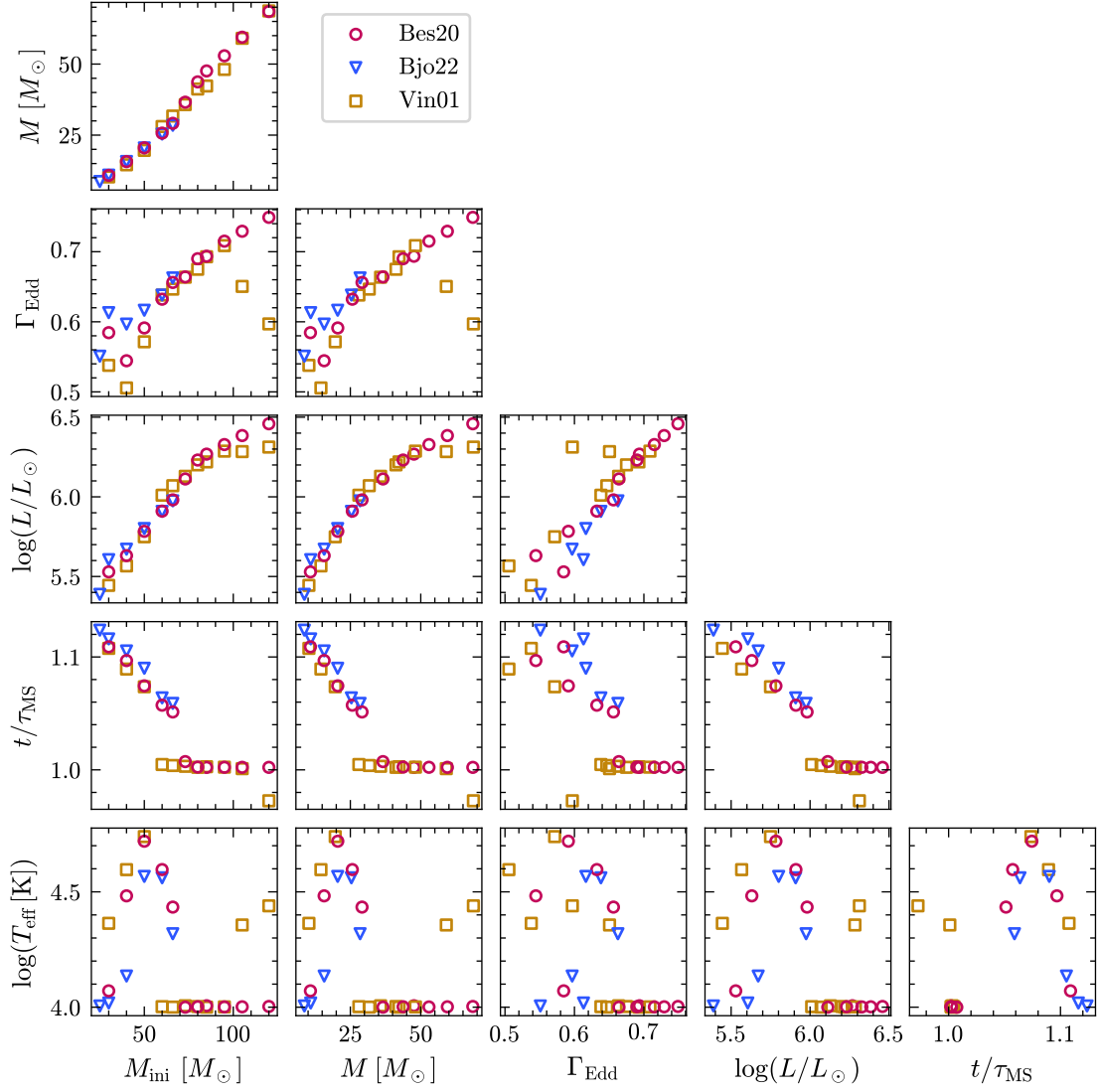


Figure 4.12: Corner plot of model parameters at the point of WR formation. The colors and shapes indicate the \dot{M}_{OB} prescription. Models that have an RSG phase use the Cro01 \dot{M}_{RSG} prescription.

after losing 49% of its mass (at $\sim 31 M_{\odot}$), whereas the Bes20 and Bjo22 models would need to lose 58% (at $\sim 25 M_{\odot}$), if we base this only on the surface hydrogen criterion. The fact that there is barely any difference between the WR formation mass of the $60 M_{\odot}$ models means that the effective temperature criterion must also play an important role in deciding the WR formation point.

Effective temperature (T_{eff}) – Initial mass (M_{ini})

There are two pathways for a star to achieve the WR criteria. Either it becomes hydrogen depleted while in the hot phase, so it is already above 10 000 K when the hydrogen drops below the critical level; or it becomes hydrogen depleted in the cool phase, so it has to first heat up again to the critical temperature before being classified as a WR. Both hydrogen depletion and surface heating tend to go hand in hand since they are both consequences of the stripping of the outer layers, but the relative strength of these effects is variable enough that both of the mentioned pathways are possible in the models. Looking at the $T_{\text{eff}}-M_{\text{ini}}$ panel, we can explore these possibilities. On this plot, models that reach the hydrogen criterion first (in the cool phase) lie on the $\log(T_{\text{eff}}[\text{K}]) = 4.0$ horizontal, which represents the threshold these models pass when they become WR. As we can see, this is the case for almost all models in the high mass loss regime except for $105 M_{\odot}$ (Vin01) and $120 M_{\odot}$ (Vin01), which lose so much mass while on the MS that they become WR before expanding to a cooler supergiant. All other models in the high mass loss regime also lose a lot of mass on the MS, but not enough to prevent them from “escaping” to the YSG phase first, where they rapidly lose more mass, exposing their small hydrogen-poor H-burning shell (zone III of the hydrogen depletion curve) and then returning to the blue as a WNL star.

Models in the low mass loss regime become RSGs or YSGs after the main sequence. Like their more massive cousins, these stars also evolve back to the blue once they have lost most of their hydrogen-burning shell, but unlike them, this region (zone III of the hydrogen depletion curve) is large and hydrogen-rich. Evolving back to hotter temperatures will therefore not directly grant them WR status, but they will first need to completely remove their H-burning shell as BSGs, becoming even hotter. Once the models achieve this, passing into zone IV of the hydrogen depletion curve, they very quickly transition through the WNL phase and directly become a hydrogen-poor WNE star.

At masses below $50 M_{\odot}$, we see that the trend reverses again and lower masses start to become WR at cooler effective temperatures. This is due to a second expansion that takes place at the onset of helium shell burning. Stars with low mass loss rates are able to reach this phase of evolution before losing enough surface hydrogen, which cools them down again before they finally lose their hydrogen shell and reach the WR phase. This is also the reason why the Bes20 and Bjo22 models become WR at a lower effective temperature than the Vin01 models at these low masses.

Time (t/τ_{MS}) – Initial mass (M_{ini})

The y -axis on this plot is the evolution time normalized by the MS timescale. The MS therefore ends at $t/\tau_{\text{MS}} = 1$, and helium burning (lasting $\sim 10\%$ of the MS) ends at around $t/\tau_{\text{MS}} = 1.1$. We see that stars in the high mass loss regime become WR stars very soon after the main sequence (due to strong YSG mass loss by DJ88) or in one case even during the MS. Stars in the low mass loss regime take longer to become WR since they first need to lose their hydrogen-rich hydrogen-burning shell. These stars become WR in the latter half of helium burning, later the lower the mass. Interestingly, the results show that stars are generally never expected to become WR within

the first half of helium burning! The separation into early-formed WR stars and late-formed WR stars is due to whether stars need to lose their entire H-burning shell or not in order to reach the hydrogen depletion threshold.

Luminosity (L) – Mass (M)

Newly formed WR stars follow a tight mass-luminosity relation, mostly regardless of MS mass loss prescription or time of formation. At the lowest masses, the [Vin01](#) models seem to become WR at a slightly lower luminosity than the weaker \dot{M}_{OB} prescriptions, which is due to these models reaching the WR phase slightly earlier in the evolution and thus at a smaller mean molecular weight μ . The [Vin01](#) 105 M_{\odot} and 120 M_{\odot} models are slightly less luminous at WR formation (by 0.1–0.15 dex) than the [Bes20](#) models of the same mass, since they become WR before being able to fully expand to supergiants.

Eddington parameter (Γ_{Edd}) - Mass (M)

This trend is the same as the Luminosity-Mass relation (since $\Gamma_{\text{Edd}} \sim L$), but outliers are more pronounced since the y axis is not logarithmic. Interestingly, this plot shows that WR stars are formed at a considerably higher Eddington factor than the value of 0.47 that [Bestenlehner \(2020\)](#) suggests as the transition to optically thick winds. This indicates that stars enter the optically thick wind regime before being classified as WR by our models. Since optically thick winds are observationally a defining characteristic of WR stars, this suggests that our models may in fact be spectroscopically identified as WR earlier than in our evolutionary calculations.

4.3.2 Evolution in the Hertzsprung-Russell Diagram

Based on the previously presented results, we can classify WR stars into two categories according to their formation history:

- (1) **Early-formed WR stars.** These are the most massive stars which experienced heavy mass loss during the main sequence and entered the WR phase on the MS, or quickly after the main sequence. Their direct progenitors are either O/B or YSG stars.
- (2) **Late-formed WR stars.** These are less massive stars that only form WR stars after losing their entire hydrogen shell as some point in the latter half of core helium burning. After the MS, they first spend considerable time as red and/or yellow supergiants, then evolve back to the blue as they lose more of their hydrogen shell. They then evolve to WR from the BSG phase.

We will now investigate how these two different types of WR star evolve in the HRD. As examples, I present the 30 M_{\odot} , 60 M_{\odot} and 85 M_{\odot} models on [Figure 4.13](#). All the 30 M_{\odot} models as well as the 60 M_{\odot} models with [Bjo22](#) and [Bes20](#) are in the weak MS mass loss regime and therefore late-formed WR stars, whereas the 85 M_{\odot} models and the 60 M_{\odot} model with [Vin01](#) are in the strong MS mass loss regime and thus become early-formed WR stars. Keeping in mind this distinction will help us compare these two classes with each other.

Early-formed WR stars

As discussed previously, early-formed WR stars have not yet removed their hydrogen-burning shell at the time of formation. They therefore first become WNL stars before they gradually lose more of their hydrogen. A young early-formed WR star still has the radius and luminosity of a supergiant, owing to its extended hydrogen layer. As its hydrogen-burning shell becomes more exposed, the

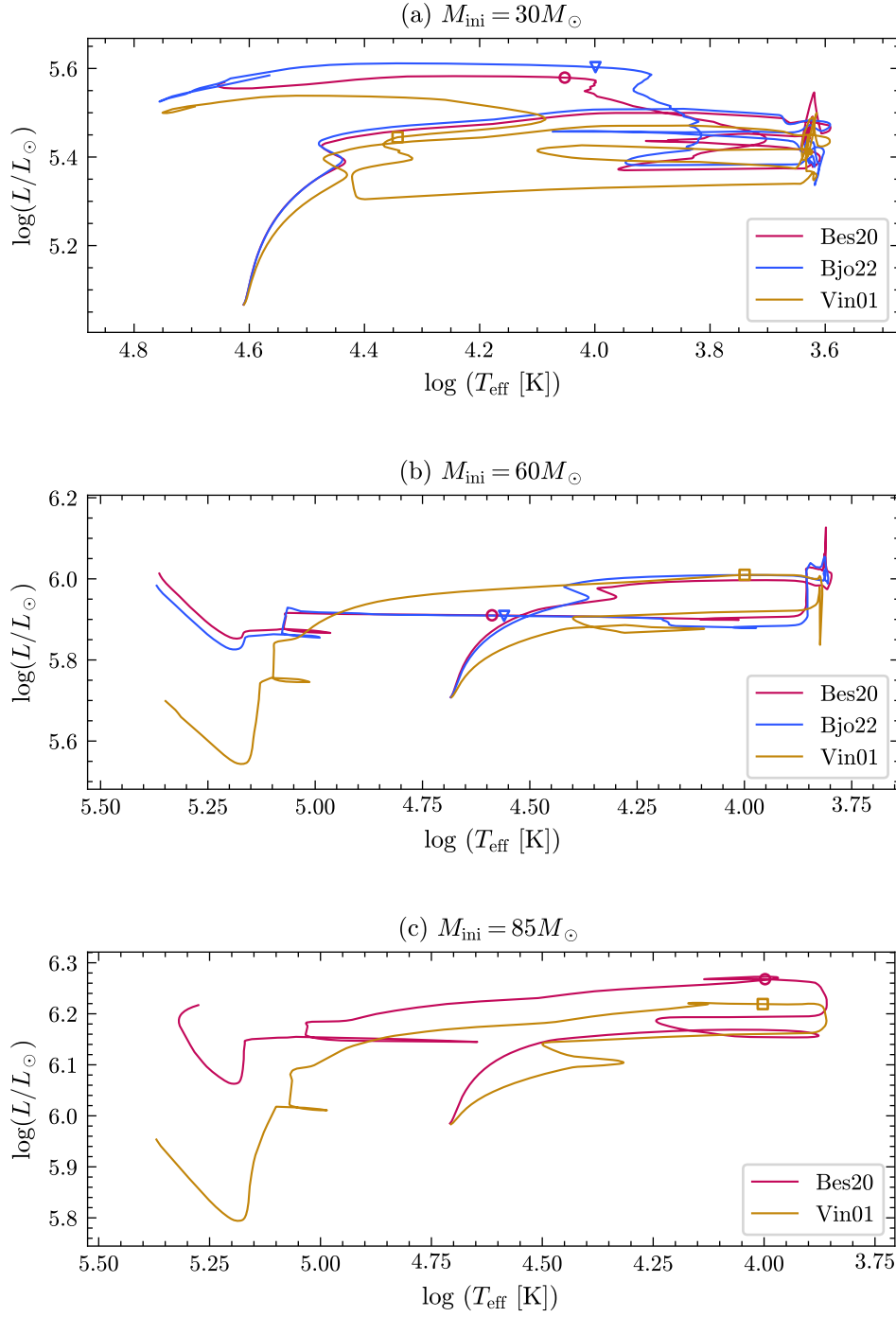


Figure 4.13: Full evolution in the HRD for models with initial masses (a) $30 M_\odot$ (with Cro01 \dot{M}_{RSG}), (b) $60 M_\odot$, (c) $85 M_\odot$. The plotted shapes mark the beginning of the WR phase on each model.

WR star travels more towards the blue, losing slightly in luminosity as it loses more mass. When the star has completely lost its hydrogen, it becomes a stripped star with a surface temperature hotter than 100 000 K. At this point, the star continues to strip down completely, losing the helium envelope above the convective helium burning core (which briefly expands just before being ejected causing a small redward spike in the HRD), and part of the carbon-enriched interior. During this process, the star remains at a relatively constant high temperature, but significantly reduces its luminosity as it progressively reduces in size to less than one solar radius. The dimming is halted by the ignition of shell helium burning, which gives the star a burst of luminosity, further increasing its surface temperature. This creates the hook-like feature at the end of the HRD tracks which is characteristic of early-formed WR stars as well as some of the earliest (most massive) late-formed WR stars (e.g. the [Bes20](#) and [Bjo22](#) 60 M_{\odot} models). The condition for this WR hook is that the star needs to be stripped of hydrogen before shell helium burning begins, i.e. mass loss needs to be fast enough relative to the nuclear timescale. The more of the helium envelope is then stripped before shell helium burning begins, the lower the luminosity of the WR hook will be (see 60 M_{\odot} models for comparison).

Late-formed WR stars

Stars in the low MS mass loss regime still possess a hydrogen-envelope of ZAMS abundances by the end of the MS. Let us follow the evolution of the 30 M_{\odot} models in the HRD as an example. When such a star moves into the YSG/RSG phase, its mass loss rate increases dramatically (by 2 to 3 orders of magnitude) (ignoring the weak \dot{M}_{RSG} prescription by [Bea20](#)), but by that time the star has formed a large convective zone due to shell hydrogen burning, pulling hydrogen-rich material deeper into the interior. While in the cool phase, the star may execute a temporary blueward evolution (known as a blue loop) as it begins to expose hotter layers, and then evolves redward again due to expansion of those newly exposed layers. As the star loses more mass, its luminosity will reduce noticeably before it finally exposes enough of its hydrogen-burning shell to move back to the blue permanently. As discussed previously, it is then not until the star has removed its entire hydrogen-burning shell completely that it finally becomes a WR star, at which point it is a stripped WNE star. At some point on the star’s blueward evolution, core helium burning ceases and shell helium burning begins, and the luminosity increases. The rest of the evolution through the later burning phases is spent losing more mass and becoming progressively hotter.

4.4 Supernova progenitors

We will now investigate the physical characteristics of the models at their endpoint, i.e. the nature of the supernova progenitors. We computed (most of) the models until the end of core carbon burning, which is the point at which the central carbon mass fraction drops below 10^{-5} . Let us first consider the location of these models in the HRD, as shown on [Figure 4.14](#). On this figure, we see that our models split clearly into several populations of supernova progenitors.

- **WC/WO stars:** These are the endpoints of most of the models with an initial mass of at least 40 M_{\odot} (using the [Cro01](#) \dot{M}_{RSG} prescription). By the time of their death, these stars have undergone so much mass loss that their surfaces are mainly carbon and oxygen with only $\sim 20\%$ helium. They have exposed their helium-burning shell and are featuring nuclear fusion close to their surface, making them extremely hot and bright.
- **WR supergiants:** These two stars are the 105 M_{\odot} and 120 M_{\odot} models using the [Bes20](#) \dot{M}_{OB} prescription. Structurally, they are similar to the other WC/WO stars, but have a

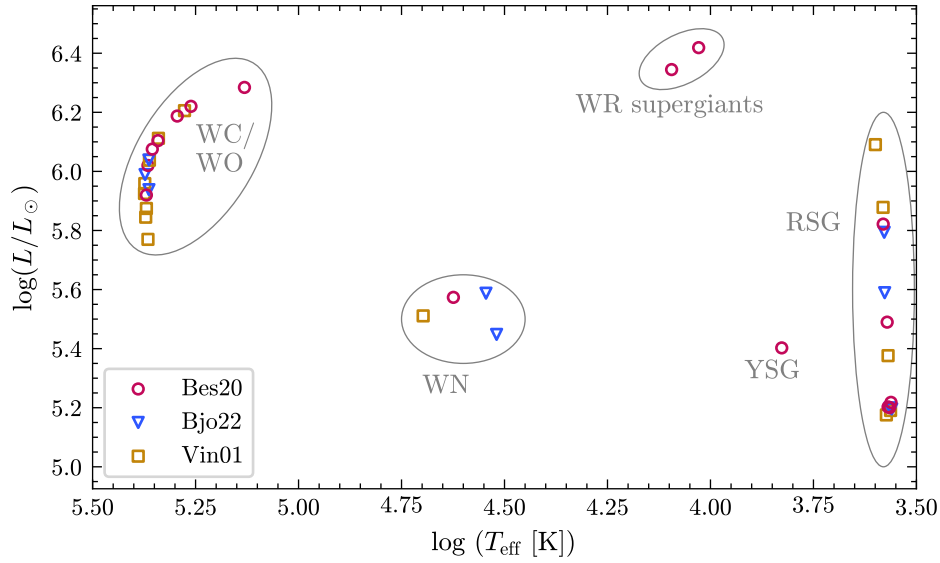


Figure 4.14: HRD showing the evolutionary endpoints of the models that were computed until the end of core carbon burning. Labeled ellipses show different populations of supernova progenitors.

higher mass ($37 M_{\odot}$ and $43 M_{\odot}$, respectively). The exposure of the helium-burning shell of such a massive star causes a rapid inflation of the atmosphere to supergiant size. However it is unclear whether such an effect is physical or just a consequence of the way the stellar atmosphere is treated by GENEC. In reality, it is possible that this rapid inflation would just qualify as normal mass loss.

- **WN stars:** These are the least massive WR stars in our sample, i.e. the $30 M_{\odot}$ models with [Cro01](#) \dot{M}_{RSG} as well as the $25 M_{\odot}$ model with [Cro01](#) \dot{M}_{RSG} and [Bjo22](#) \dot{M}_{OB} . These stars have lost their H-burning shell, but still have an envelope made of the products of core hydrogen-burning below, composed of about 99% helium and 1% nitrogen. Their helium-burning shell is still substantially covered, resulting in a cooler surface than the WC/WO stars.
- **RSG stars:** These are the endpoints of the least massive stars, as well as all the stars using the [Bea20](#) \dot{M}_{RSG} prescription. Their mass loss was too weak to significantly expose the H-burning shell and evolve back to the blue. They die as a cool supergiant with only a slightly hydrogen-depleted surface, still consisting of 50–65% hydrogen.
- **YSG stars:** Only one model finished at this point ($25 M_{\odot}$, [Bes20](#) \dot{M}_{OB} , [Cro01](#) \dot{M}_{RSG}), probably as a transition phase from RSG to WR. It has depleted most of its surface hydrogen (to $\sim 20\%$) and was now in the process of losing its hydrogen-burning shell and evolving back to the blue.

[Figure 4.15](#) shows the mass of the models at the end of central carbon burning. If we compare this to the models at the TAMS ([Figure 4.4](#)), we see that the most significant mass loss happens in the post-MS evolution (except the models using the weak [Bea20](#) \dot{M}_{RSG}). Both the RSG phase as well as the WR phase are typically characterized as having a high mass loss rate compared to the main sequence. Nevertheless, we have seen that the mass loss rate during the main sequence significantly influences the different paths for evolution until the end, despite being much weaker. Of course, the total mass loss will be very dependent on the mass loss prescriptions used for the

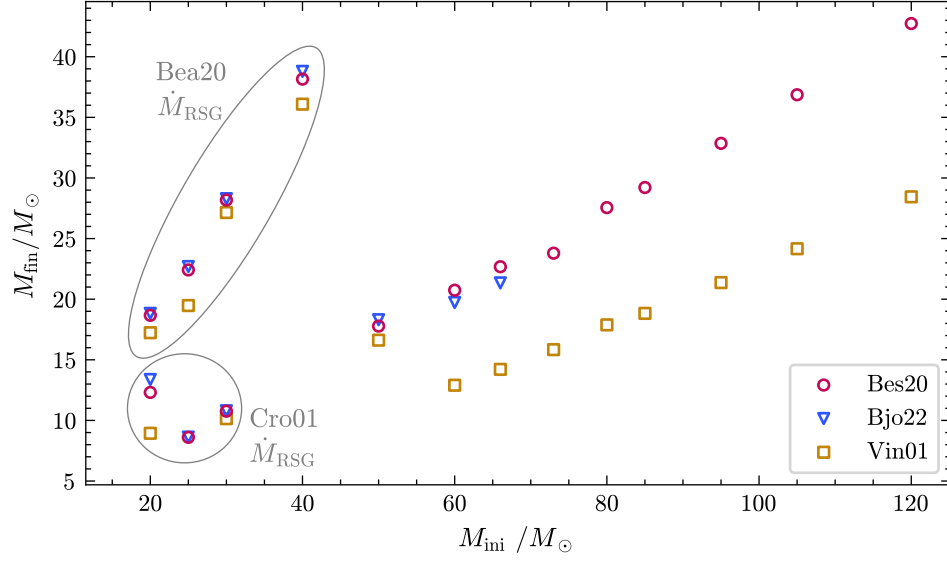


Figure 4.15: Final mass of the models as a function of initial mass.

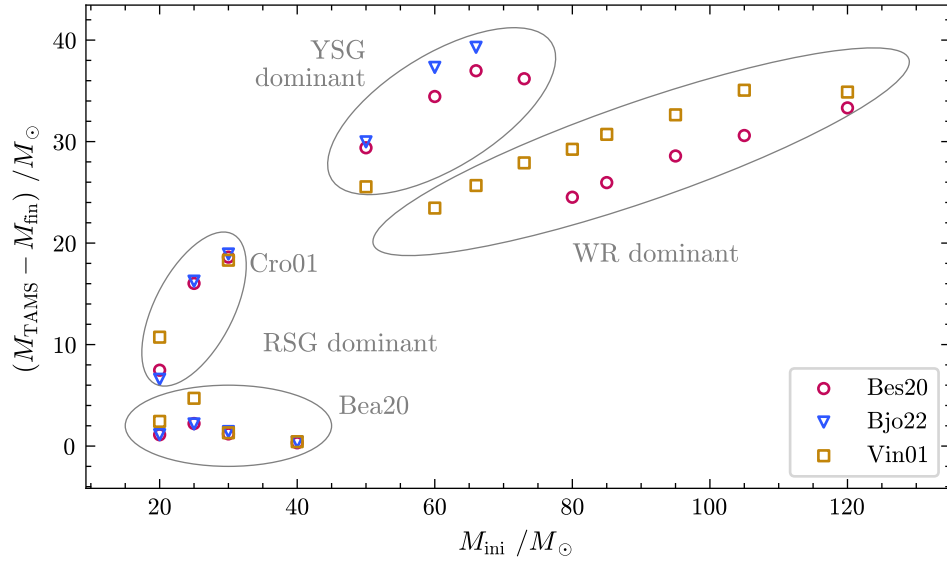


Figure 4.16: Total mass lost in the models after the main sequence as a function of initial mass. The models separate into groups depending on which phase dominates the post-MS mass loss.

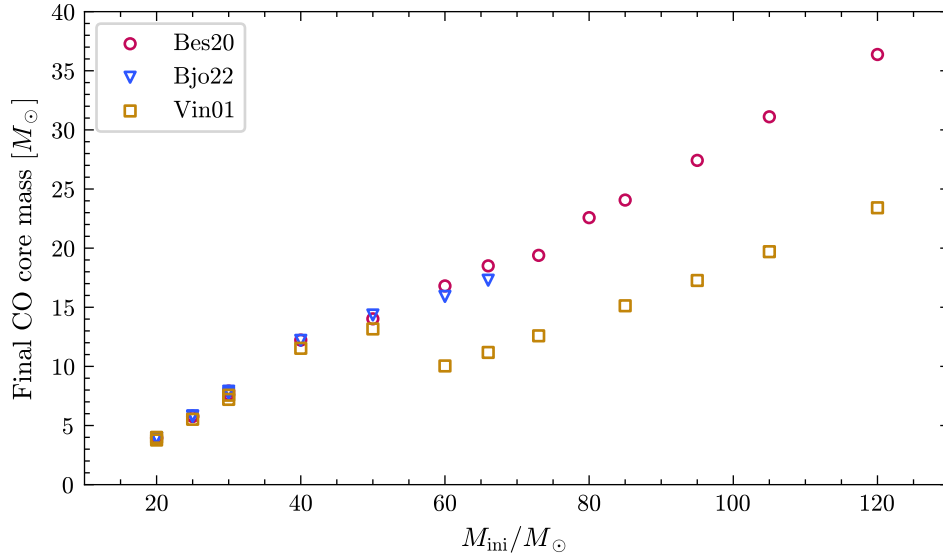


Figure 4.17: Mass of the CO core (whose boundary is defined as the layer where helium abundance increases above 1% when starting from the center outwards) at the end of central carbon burning. For models with an RSG phase, the results from both \dot{M}_{RSG} prescriptions are shown, but their final core masses are so similar regardless of the mass loss prescriptions that the scatter points are indistinguishable.

post-MS phases. Since those include any combination of RSG prescription, O/B prescription, WR prescriptions, and the default DJ88, and the star’s state has been influenced by MS mass loss, there are too many variables to make any solid conclusions on the effect of any one mass loss prescription in the post-MS evolution. Instead, we can consider the general influence of the various evolutionary phases of the stars on their mass loss. For example, we know that stars experience strong mass loss in the YSG phase and that the mass loss rate generally scales with luminosity/mass. One interesting consequence of this is that there is no longer a trace of the two MS mass loss regimes for Bes20 when looking at the final masses. This is due to the 50–73 M_{\odot} models of this prescription entering the YSG phase at a high mass, activating strong mass loss which compensates for the lower mass loss in the main sequence. Higher mass models stay in the YSG phase for only a very short time before becoming WR stars, whose mass loss rate is generally lower. Figure 4.16 shows the mass lost in the post-MS evolution by the models. It clearly exhibits a separation of the models into different groups depending on which post-MS phase dominates the mass loss of the evolution. As we can see, the most massive stars of the low MS mass loss regime spend the most time in the YSG phase, on which we apply the highest mass loss rate. They therefore lose the most mass after the main sequence, even more than the most massive WR stars in our sample.

Finally, let us consider the core mass at the end of central carbon burning. Specifically, we define the CO core of a star as being the region where hydrogen abundance is zero and helium abundance is below 1%. The mass of this region, shown for the models in Figure 4.17, is an important predictor of the mass and type of supernova remnant. Interestingly, the results show that the final CO core mass of stars with initial masses between 20–40 M_{\odot} does not depend on the mass loss rates applied throughout the evolution. This is somewhat surprising, since the two mass loss prescriptions we apply for the RSG phase differ by several orders of magnitude and produce evolved stars of very different total masses (see Figure 4.15). Evidently, mass loss during the RSG phase simply has the effect of removing the hydrogen-rich envelope, without having any influence

on core structure. This contrasts significantly with MS mass loss, which can indeed affect the interior structure of stars, but is too weak in the low mass range to have an impact on final CO core mass.

4.5 Stellar populations

To conclude the presentation of the results, let us briefly analyze some implications of the results for stellar populations. Here, I will focus on the results that can be directly inferred from the single star evolution models, although this topic would certainly deserve much more attention by using dedicated stellar population synthesis models.

An important characteristic of stellar populations is the relative abundances of stars in different evolutionary phases, namely MS, RSGs, YSGs, BSGs and the various WR types. I will now present how we can derive this quantity from the models. For simplicity, let us consider a population whose star formation rate (SFR) has been constant over a timescale longer than the typical lifetime of a massive star, resulting in a population that is in equilibrium. Let dN be the number of new stars forming per unit time within an initial mass interval dM_{ini} , and dN_i the number of stars of this mass interval currently in the evolutionary phase i . If the timescale for phase i is denoted by τ_i , we obtain $dN_i = \tau_i dN$, and since both τ_i and dN are generally functions of the initial mass, we can rewrite this as

$$dN_i = \tau_i(M_{\text{ini}}) \frac{dN}{dM_{\text{ini}}} dM_{\text{ini}}. \quad (4.5)$$

The term dN/dM_{ini} describes the probability distribution of initial masses at star formation and is also known as the *initial mass function* (IMF). It is commonly assumed as the power law given by [Salpeter \(1955\)](#) with an exponent of -2.35 , making more massive stars form more rarely than low-mass stars. The total number N_i of stars in phase i across all initial masses is then obtained by integrating [Equation 4.5](#) over the initial mass range of the population,

$$N_i = K \int \tau_i(M_{\text{ini}}) M_{\text{ini}}^{-2.35} dM_{\text{ini}}, \quad (4.6)$$

where K is some proportionality constant that normalizes the IMF to a given star formation rate. Since we are only interested in the N_i relative to each other, this constant is irrelevant. The consequence of this result is that we can visualize N_i as the area under the curve $\tau_i(M_{\text{ini}})$ where the x -axis is scaled so that $dx = M_{\text{ini}}^{-2.35} dM_{\text{ini}}$. This is shown in [Figure 4.18](#) as a stacked line graph using the post-MS phase timescales $\tau_i(M_{\text{ini}})$ obtained from the models. It is important to note that the timescales are shown cummulative, so that there is no information about the order in which the different phases are traversed. The relative abundances of stars in different phases (including the MS) in a population of 20–120 M_{\odot} stars with constant SFR is shown in [Table 4.4](#).

The results nicely summarize some conclusions of the previous analysis. Firstly, regardless of \dot{M}_{OB} , stars in the low MS mass loss regime spend more time as YSGs, during which time they are removing their large hydrogen-envelope. Secondly, these stars also spend less time as hydrogen-containing WNL, since they transition quickly from BSG to WNE when they remove their H-burning shell. Comparing the different mass loss prescriptions with each other, we first notice that the [Bea20](#) \dot{M}_{RSG} results in a much higher abundance of RSGs than [Cro01](#), as expected. Then, we see that in the low mass loss regime with [Cro01](#) \dot{M}_{RSG} , the [Vin01](#) \dot{M}_{OB} produces more BSGs than the [Bes20](#) \dot{M}_{OB} , due to its higher MS mass loss rate making the RSG phase shorter. Finally, the figure also shows that longer total post-MS lifetimes seem to be favored by higher

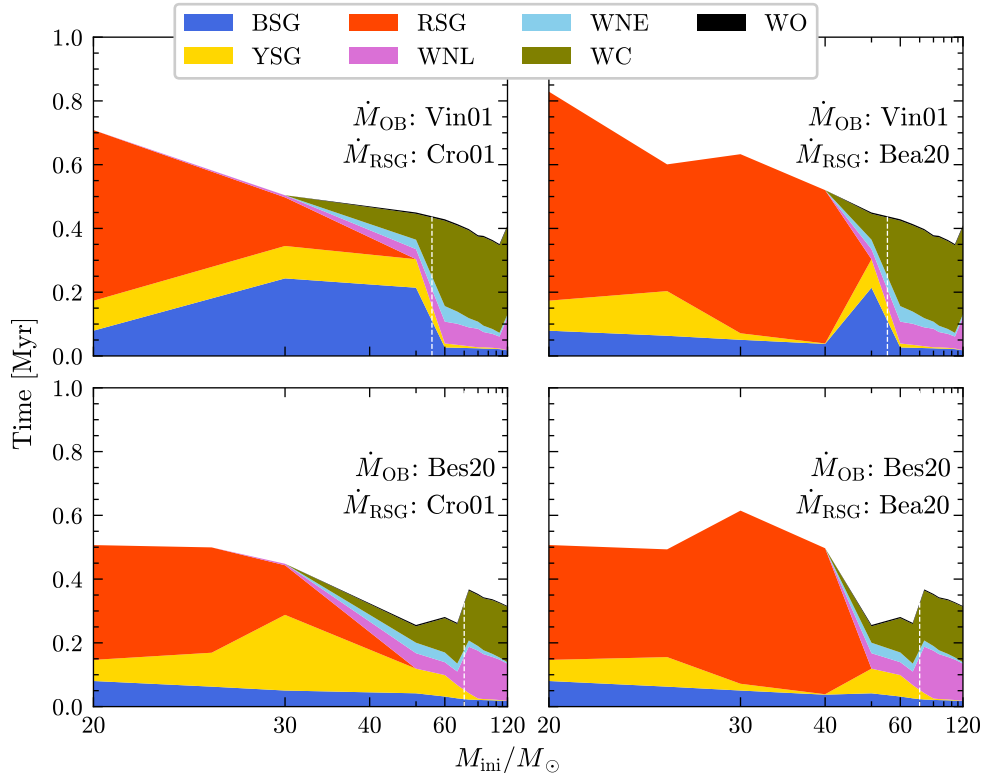


Figure 4.18: Cumulative timescales of the post-MS evolutionary phases as a function of initial mass for different combinations of \dot{M}_{OB} and \dot{M}_{RSG} prescriptions. The x -axis is scaled using an initial mass function so that the area of each region is proportional to the fraction of stars in the corresponding phase in a population of constant star-formation rate. (See main text for details.) The dashed white lines represent the approximate location of the boundary between the low mass loss regime and the high mass loss regime of the MS, according to Figure 4.4.

Phase	Relative abundance [%]			
	Vin01 \dot{M}_{OB}		Bes20 \dot{M}_{OB}	
	Cro01 \dot{M}_{RSG}	Bea20 \dot{M}_{RSG}	Cro01 \dot{M}_{RSG}	Bea20 \dot{M}_{RSG}
MS	91.07	90.20	92.77	91.82
RSG	3.14	6.28	2.96	5.39
BSG	2.72	1.12	0.91	0.88
YSG	1.37	1.01	2.01	0.84
WR	1.71	1.39	1.37	1.08
WNL	0.34	0.24	0.51	0.39
WNE	0.20	0.14	0.18	0.12
WC	1.14	0.99	0.65	0.55
WO	0.03	0.02	0.03	0.02

Table 4.4: Relative abundances of different types of stars in a population of stars of initial masses 20–120 M_{\odot} using different mass loss rates, assuming the IMF from Salpeter (1955) and constant SFR.

MS mass loss rates but lower RSG mass loss rates. This can also be explained: higher MS mass loss lowers the mass of the star at the onset of post-MS evolution, making it run more slowly. Conversely, higher RSG mass loss makes the helium-burning core convective region shrink faster, resulting in less fuel being available to burn and the star evolving faster through its post-MS.

CHAPTER 5

CONCLUSION

5.1 Summary

In this project, I aimed to investigate the effects of mass loss on the evolution of massive stars, focusing on the impact of mass loss during the main sequence (MS), when the stars appear as hot O/B-type stars. For this purpose, I implemented different prescriptions for calculating the mass loss rate into the Geneva stellar evolution code (GENEC) and computed a grid of stellar evolution models of different initial masses from the zero-age main sequence (ZAMS) until the end of central carbon burning. The results show striking differences in evolution that arise by varying the main sequence mass loss rate. In the analysis, I systematically studied the different phases of evolution and how they relate to the O/B mass loss, beginning with the main sequence itself, followed by the Wolf-Rayet (WR) phase and ending with supernova progenitors. I finally briefly presented some implications of the results for populations of massive stars.

Mass loss during the MS acts early and over long timescales. The results show that it affects the evolution in two ways. Firstly, it leads directly to the removal of the outer layers of the star, beginning with the hydrogen envelope. This has the general consequence of exposing metals on the surface and increasing the effective temperature once enough material has been removed. In this regard, mass loss acts in the same way in the MS as it would during any other phase. However, MS mass loss has been shown to have a second effect which is unique to this phase and acts more indirectly, namely through its connection with the formation and evolution of interior convective zones. We have seen that mass loss directly affects the size of the convective core during the main sequence. But more importantly, MS mass loss is almost the sole determinant of the mass a star has when it inflates to the supergiant phase, which arguably marks the most dramatic structure change in the life of a massive star. It is at this time that the star forms a hydrogen-burning shell with a convective zone above it, and that the core contracts and begins to burn helium in the center. The appearance of these structures is directly dependent on MS mass loss and will go on to determine the entire subsequent evolution of the star. After this critical transition at the end of the main sequence, mass loss loses its connection to the evolution of interior convective zones and its effect becomes much more straightforward. For this reason, we have found that the final core mass of a massive star depends much more on the mass loss during the main sequence than the mass loss during the post-MS phases, despite the MS mass loss rate being the weakest.

The specific O/B mass loss prescriptions we have explored show a clear separation into two distinct mass loss regimes of the main sequence. (Except for [Bjo22](#), which is only valid for the lower part of the mass range.) The results show that the qualitative evolution of a star depends

much more on the regime that it falls into, rather than the specific prescription itself. We have discussed small quantitative differences that are due to small changes in \dot{M}_{OB} such as the minimum temperature during the main sequence, or the luminosity of the WR hook in the HRD. However, the general evolutionary path from the ZAMS to the endpoint is a consequence of the mass loss regime, and thus the point of interest of each mass loss prescription is its regime transition mass rather than the mass loss rate itself. In summary, the results show the following main evolutionary paths.

- (a) O/B \rightarrow RSG
- (b) O/B \rightarrow RSG/YSG \rightarrow BSG \rightarrow WNE (\rightarrow WC/WO)
- (c) O/B \rightarrow WNL \rightarrow WNE \rightarrow WC/WO

Stars with the lowest initial masses in our grid will experience type (a) evolution due to their mass loss being too low to escape from the RSG phase back to the blue. The mass limit between type (a) and type (b) evolution (i.e. the minimum mass to form WR stars) depends on the mass loss experienced during the RSG phase. The strong \dot{M}_{RSG} by [Cro01](#) places this limit at $\sim 25\text{--}30 M_{\odot}$, whereas models using the much weaker [Bea20](#) RSG winds follow type (a) tracks up to an initial mass of $40 M_{\odot}$, which is the upper limit for RSG formation.

Type (b) evolution corresponds to the models that have strong enough mass loss to form WR stars, but are still located in what I have referred to as the low mass loss regime. They spend a considerable amount of time as cool RSGs/YSGs and then evolve back to the blue and become hydrogen-depleted WNE stars, and eventually nitrogen-depleted WC/WO stars if the mass loss is strong enough. Since these stars only enter the WR phase in the second half of core helium, I have called them late-formed WR stars.

Models with type (c) tracks evolve to the WR phase directly from the main sequence, only briefly passing through the YSG phase for a few thousand years. These models become WR stars close to the beginning of core helium-burning and I have therefore called them early-formed WR stars, forming as WNL stars while hydrogen still remains on the surface. The transition mass between type (b) and type (c) evolution corresponds to the limit between the low and the high MS mass loss regime, which depends on the chosen \dot{M}_{OB} prescription. The [Bes20](#) prescription puts this limit at $\sim 70 M_{\odot}$, and we recall that this transition mass is a robust prediction of this mass loss model. For [Vin01](#), the transition mass is lower, being closer to $\sim 40\text{--}50 M_{\odot}$.

As a result of the different evolutionary tracks determined by mass loss, we obtained several different populations of potential supernova progenitors, which can be grouped into WN stars, WC/WO stars and RSGs. One model also finished as a YSG, but this model seemed to be in transition to the WR phase, making this kind of SN progenitor potentially rare.

5.2 Discussion and Outlook

The conclusions presented in this study are based on results obtained from evolutionary models of single massive stars at solar metallicity and without rotation. Although the limits of this parameter space may impose constraints on the observability of the predicted phenomena, we should nonetheless consider the applicability of the results on domains that were not directly explored in the simulations. In the following, we discuss several aspects of stellar evolution and our models with the goal of evaluating the limitations and the impact of our conclusions.

Metallicity

The presence of metals in the atmospheres of stars has the general effect of increasing the opacity of the medium due to the greater number and strength of metallic absorption lines. This induces greater radiation pressure and therefore greater mass loss. Often, a metallicity dependence is included in mass loss prescriptions in the form of a power law $\dot{M} \sim Z^a$, as is the case for [Vin01](#) and [Bjo22](#). The metallicity dependence of [Bes20](#) is less direct. In this prescription, the mass loss depends on the electron scattering Eddington parameter, with a force-multiplier parameter α that supposedly corrects for the contribution of metallic lines to the total opacity. For implementation in GENECE, we have used values for α and the mass loss rate scale $\log \dot{M}$ as calibrated by [Brands et al. \(2022\)](#) on LMC stars. These stars have a metallicity of around half of the sun’s and therefore exhibit a mass loss rate that is lower than galactic O/B stars by a factor of around 1.4–1.8, assuming metallicity scaling of with an exponent of around 0.5–0.85 ([Kudritzki & Puls, 2000](#); [Vink et al., 2001](#)). Since we have directly applied this prescription at galactic metallicity without adjustment, we expect the resulting mass loss rate to be underestimated by this factor. However, we do not expect this to impact the results significantly. Importantly, the transition mass between the optically thin and optically thick regimes remains unaffected by this consideration.

In general, it is reasonable to propose that the studied effects of mass loss remain qualitatively similar at metallicities that are close to the solar value in orders of magnitude, so we should expect similar results for LMC and even perhaps SMC metallicity. However, it may still be interesting to study even small effects of varying the metallicity in order to obtain a more precise model of the evolution of massive stars outside the Milky Way. The large observational sample of WR stars in the LMC and the fact that our version of the [Bes20](#) mass loss recipe is calibrated on LMC data are motivation enough to study this metallicity more closely. In our upcoming paper ([Josiek & Ekström, in prep.](#)), we will complement the present grid of models with ones at LMC metallicity in order to explore the role of metallicity in linking mass loss to stellar evolution, specifically that of WR stars.

Binarity and rotation

Most massive stars experience a binary interaction at some point during their lives ([Sana et al., 2012](#)), and as many as 30% of massive main sequence stars are the product of binary mergers ([de Mink et al., 2014](#)). Stars in binaries can lose (and gain) mass by transfer to and from their companion, which is an effect that is not treated within the single-star evolution scheme. The mass flow induced by binarity may dominate (by far) the effect of radiatively driven winds, which makes it very difficult to apply the results of the present study to real populations of massive stars. Furthermore, binary interaction also significantly influences the rotational behavior of stars, especially in the event of a merger, where the entire orbital angular momentum is transferred into the rotational angular momentum of the merger product. Rotation is clearly closely linked to mass loss. Rotating stars have lower surface gravity at the equator than at the poles, and they are also cooler on the surface at the equator than at the poles. This anisotropy in the stellar surface parameters introduces an entirely new layer of complexity into the treatment of mass loss, even for single stars. When measuring mass loss rates, the angle of observation and the uncertainty thereof must play a role in interpreting the observational data, and rotating stellar models must be at least two-dimensional in order to include both radial and latitudinal variation of wind parameters. Furthermore, rotation not only affects mass loss, but also other aspects of stellar evolution such as convective mixing within the star ([Maeder & Meynet, 2000](#)), which we have found to be a crucial link between mass loss and evolution.

We see that the binarity and rotation of massive stars could impact their evolution in a way that is too complex to extrapolate from the present non-rotating single-star models. The results from this work should therefore be regarded as an exploration of the physical mechanisms relating mass loss and stellar evolution, which are in theory universal, but we remain inconclusive regarding their ability to make predictions about stars that do not evolve in the non-rotating single-star picture due to the constraints on our parameter space.

Existence of the mass loss regime change

Our results show a clear separation of the models into two main sequence mass loss regimes for the Bes20 and Vin01 prescriptions, and many subsequent conclusions follow this divide. Although both of these prescriptions justify the resulting regime changes, we may question whether they truly represent reality. Björklund *et al.* (2022) argue for the absence of the iron bistability jump found in Vin01 with their hydrodynamically consistent wind models. However, due to the constraints of their parameter space to stars smaller than $80 M_{\odot}$, it is unclear whether their prescription (Bjo22) may produce a regime change for other reasons for stars of higher masses. The regime change between optically thin and optically thick winds represented as different $\dot{M}(\Gamma_{\text{Edd}})$ dependencies in the Bes20 prescription seems to be more strongly supported by observational studies such as Bestenlehner *et al.* (2014) and Brands *et al.* (2022).

Theoretical definition of WR stars

For this work, we have defined WR stars via a strict threshold of surface temperature and hydrogen mass fraction. Based on this definition, we have found that the classification of a WR star as early-formed or late-formed depends directly on the hydrogen content of its convective hydrogen shell with respect to the threshold value. If the hydrogen shell is hydrogen-rich, the WR star forms late, whereas if the hydrogen shell is hydrogen-poor, the WR star forms early. Shifting the WR surface hydrogen threshold to a higher value (e.g. 0.4 as it is sometimes defined) would simply lower the mass limit between early-formed and late-formed WR stars. Early-formed WR stars would form earlier, and the remaining late-formed WR stars would form at about the same moment, since the drop from hydrogen-rich to hydrogen-depleted happens very fast when the hydrogen-burning shell is removed and thus the exact hydrogen threshold value does not matter. In general, we would reach similar conclusions regarding the formation and evolution of WR stars if the threshold were chosen differently.

The reality of WR stars is not a simple question of surface hydrogen abundance and effective temperature. In GENEC, we choose to apply strong WR-type winds for models that reach these defined thresholds, which implies that a simulated spectrum would indeed probably be classified as WR. We effectively assume that a star is WR in order to apply a corresponding mass loss rate, whereas a spectroscopic WR-type classification is really a consequence of mass loss. As a result, we automatically exclude the possibility of forming hot hydrogen-poor stars with optically thin winds. These stripped helium stars exist, and their mass loss is significantly lower than that of WNE-type stars (Vink, 2017). Our models do not differentiate between stripped stars and WR stars. In fact, one of the main characteristics of late-formed WR stars is that they are stripped.

For more accurate modeling of WR stars and their evolution, it would be beneficial to use mass loss prescriptions for hydrogen-poor stars that can produce optically thin as well as optically thick winds. Ideally, spectroscopic WR stars should arise naturally from evolutionary calculations without having to first apply dedicated WR mass loss prescriptions. In this regard, it would be interesting to lay some spectral models on the Bes20 evolutionary tracks, since we kept this

prescription valid for hydrogen-poor (“WNL”) stars without applying special WR mass loss rates. In any case, it may be useful to revise the theoretical definition of WR stars in models in order to more closely represent reality. Since WR stars are observationally characterized as having a large extended atmosphere that obscures the stellar surface, we suggest exploring a definition of WR stars based on mass loss history in order to produce such thick ejecta.

Observability

In the study of massive stars, observational constraints of evolutionary models often come from population surveys, with key indicators being the abundance ratios between different types of stars, e.g. WR/O, BSG/RSG, and so on (See [Eggenberger et al., 2002](#); [Wagle et al., 2020](#)). In [section 4.5](#), I presented a method of approximating these abundances from the evolutionary models without the need for a population synthesis. I have discussed different ways in which the mass loss rate can impact these ratios, but have refrained from making direct comparisons with observations. The main reason for which these results cannot be directly compared to observations is the constraint on the initial masses. There are O/B-type stars below $20 M_{\odot}$ which we excluded from this study because of their relatively predictable evolution (MS→RSG). However, because of the IMF, these stars outnumber their more massive counterparts and need to be accounted for if one wishes to obtain “realistic” ratios.

As mentioned previously, the conclusions of this work should not be taken as a prediction of stellar population characteristics, but rather as an analysis of the physical link between mass loss and evolution. The effects explored here (such as abundance ratios) could potentially be used as indicators for the validity of certain mass loss prescriptions, but this cannot be done without more complete model grids. Observations could also be used to compare and calibrate the mass loss prescriptions directly so that their implementation in stellar evolution codes is more robust.

Impact

This work offers insights into the formation and evolution mechanisms of (theoretical) Wolf-Rayet stars from the single-star perspective. By systematically investigating the structure of massive stars throughout all of their evolutionary phases, we have obtained a deep understanding of the role of mass loss during the main sequence and post-MS phases. The mass loss rate is one of the major remaining uncertainties in single-star evolution codes, and thus it is important to consider a wide range of possible mass loss scenarios. The different mass loss rates studied here differ from each other by around one order of magnitude (even more for the RSG phase), which gives rise to significant differences in the possible evolution of massive stars.

Based on the present results and conclusions, we are able to predict certain late-stage evolutionary characteristics of massive stars such as WR formation channel, final core mass and evolutionary endpoint as well as approximate a full track in the HRD, just by considering a model’s main sequence evolution with a given mass loss rate. This can be useful when evaluating new mass loss prescriptions, since it allows us to characterize their effects on the full evolution of massive stars and their populations without the need to compute the full tracks explicitly.

Open problems and further work

To conclude, let us summarize some key questions that remain unanswered in this project which could be the basis of subsequent research. The following points recapitulate the limitations of this work that were already discussed, and expose some ideas for further exploration.

- A wider parameter space for the models could be investigated. This could include more metallicities, rotation rates, initial masses, as well as binary (and higher order) models. Given the current state of stellar evolution codes, a full and detailed study of all of these effects is not currently realistic, but individual models could be explored.
- The impact of the validity domains of the mass loss prescriptions in the evolution codes can be studied. It may be beneficial to couple the validity domains to evolutionary phases rather than stellar parameters in order to make different prescriptions more comparable to each other. The application of WR mass loss rates should be revised, since the current implementation does not leave room for stripped stars with weak winds.
- Studies of spectra simulated from evolutionary tracks could be undertaken to help strengthen the link between spectral classification and stellar evolution, and give rise to an improved theoretical definition of WR stars.
- With a model grid spanning the full mass range of massive stars, a full picture of stellar populations could be obtained, which could then be compared to real observational surveys of massive stars. The properties of observed WR and O populations could then be used as constraints on the main sequence (and post-MS) mass loss rate prescriptions, taking into account the results from the present work.
- Attempts could be made to couple hydrodynamic stellar atmosphere models to stellar evolution models in order to compute surface properties such as the mass loss rate in a self-consistent way to forego the reliance on prescriptions.

Some of these points will be addressed more in the upcoming paper relating to this work, and I will explore the last point as part of my upcoming PhD position in the group of Andreas Sander in Heidelberg starting in September this year.

REFERENCES

- (1) Abbott, D. C. & Conti, P. S. Wolf-rayet stars. *ARA&A* **25**, 113–150 (1987).
- (2) Asplund, M. *et al.* *The Solar Chemical Composition in Cosmic Abundances as Records of Stellar Evolution and Nucleosynthesis* (eds Barnes Thomas G., I. & Bash, F. N.) **336** (2005), 25.
- (3) Beasor, E. R. & Davies, B. The evolution of red supergiants to supernova in NGC 2100. *MNRAS* **463**, 1269–1283 (2016).
- (4) Beasor, E. R. & Davies, B. The evolution of red supergiant mass-loss rates. *MNRAS* **475**, 55–62 (2018).
- (5) Beasor, E. R. *et al.* A new mass-loss rate prescription for red supergiants. *MNRAS* **492**, 5994–6006 (2020).
- (6) Bestenlehner, J. M. *et al.* The VLT-FLAMES Tarantula Survey. XVII. Physical and wind properties of massive stars at the top of the main sequence. *A&A* **570**, A38 (2014).
- (7) Bestenlehner, J. M. Mass loss and the Eddington parameter: a new mass-loss recipe for hot and massive stars. *MNRAS* **493**, 3938–3946 (2020).
- (8) Björklund, R. *et al.* New predictions for radiation-driven, steady-state mass-loss and wind-momentum from hot, massive stars III. Updated mass-loss rates for stellar evolution. *arXiv e-prints*, arXiv:2203.08218 (2022).
- (9) Böhm-Vitense, E. *Theory of the hydrogen convection zone in Aerodynamic Phenomena in Stellar Atmospheres* (ed Thomas, R. N.) **12** (1960), 338–345.
- (10) Brands, S. A. *et al.* The R136 star cluster dissected with Hubble Space Telescope/STIS. III. The most massive stars and their clumped winds. *A&A* **663**, A36 (2022).
- (11) Castor, J. I. *et al.* Radiation-driven winds in Of stars. *ApJ* **195**, 157–174 (1975).
- (12) Chabrier, G. & Baraffe, I. Structure and evolution of low-mass stars. *A&A* **327**, 1039–1053 (1997).
- (13) Crowther, P. A. *et al.* Physical parameters and wind properties of galactic early B supergiants. *A&A* **446**, 279–293 (2006).
- (14) Crowther, P. A. *Stellar Winds from Massive Stars in The Influence of Binaries on Stellar Population Studies* (ed Vanbeveren, D.) **264** (2001), 215.

- (15) De Jager, C. *et al.* Mass loss rates in the Hertzsprung-Russell diagram. *A&AS* **72**, 259–289 (1988).
- (16) De Mink, S. E. *et al.* The Incidence of Stellar Mergers and Mass Gainers among Massive Stars. *ApJ* **782**, 7 (2014).
- (17) Dessart, L. *et al.* Helium stars exploding in circumstellar material and the origin of Type Ibn supernovae. *A&A* **658**, A130 (2022).
- (18) Dessart, L. *et al.* Radiative-transfer models for explosions from rotating and non-rotating single WC stars. Implications for SN 1998bw and LGRB/SNe. *A&A* **603**, A51 (2017).
- (19) Eggenberger, P. *et al.* The blue to red supergiant ratio in young clusters at various metallicities. *A&A* **386**, 576–582 (2002).
- (20) Eggenberger, P. *et al.* The Geneva stellar evolution code. *Ap&SS* **316**, 43–54 (2008).
- (21) Eggenberger, P. *et al.* Grids of stellar models with rotation. VI. Models from 0.8 to 120 M_{\odot} at a metallicity $Z = 0.006$. *A&A* **652**, A137 (2021).
- (22) Ekström, S. *et al.* Grids of stellar models with rotation. I. Models from 0.8 to 120 M_{\odot} at solar metallicity ($Z = 0.014$). *A&A* **537**, A146 (2012).
- (23) ESA Science & Technology. *A history of astrometry - Part I: Mapping the sky from ancient to pre-modern times* ESA. <https://sci.esa.int/web/gaia/-/53196-the-oldest-sky-maps>.
- (24) Gaia Collaboration. Gaia Early Data Release 3. Summary of the contents and survey properties. *A&A* **649**, A1 (2021).
- (25) Gal-Yam, A. *et al.* A Wolf-Rayet-like progenitor of SN 2013cu from spectral observations of a stellar wind. *Nature* **509**, 471–474 (2014).
- (26) Georgy, C. *et al.* Grids of stellar models with rotation. II. WR populations and supernovae/-GRB progenitors at $Z = 0.014$. *A&A* **542**, A29 (2012).
- (27) Georgy, C. *et al.* Grids of stellar models with rotation. III. Models from 0.8 to 120 M_{\odot} at a metallicity $Z = 0.002$. *A&A* **558**, A103 (2013).
- (28) Gräfener, G. & Hamann, W. R. Mass loss from late-type WN stars and its Z-dependence. Very massive stars approaching the Eddington limit. *A&A* **482**, 945–960 (2008).
- (29) Groh, J. H. Early-time spectra of supernovae and their precursor winds. The luminous blue variable/yellow hypergiant progenitor of SN 2013cu. *A&A* **572**, L11 (2014).
- (30) Groh, J. H. *et al.* Progenitors of supernova Ibc: a single Wolf-Rayet star as the possible progenitor of the SN Ib iPTF13bvn. *A&A* **558**, L1 (2013).
- (31) Groh, J. H. *et al.* The evolution of massive stars and their spectra. I. A non-rotating 60 M_{\odot} star from the zero-age main sequence to the pre-supernova stage. *A&A* **564**, A30 (2014).

- (32) Hansen, C. J. & Kawaler, S. D. *Stellar Interiors. Physical Principles, Structure, and Evolution*. (1994).
- (33) Harris, C. R. *et al.* Array programming with NumPy. *Nature* **585**, 357–362 (2020).
- (34) Henyey, L. G. *et al.* A Method for Automatic Computation of Stellar Evolution. *ApJ* **129**, 628 (1959).
- (35) Henyey, L. G. *et al.* A New Method of Automatic Computation of Stellar Evolution. *ApJ* **139**, 306 (1964).
- (36) Hunter, J. D. Matplotlib: A 2D graphics environment. *Computing in Science & Engineering* **9**, 90–95 (2007).
- (37) Josiek, J. & Ekström, S. Impact of mass loss on the formation and evolution of Wolf-Rayet stars (in prep.).
- (38) Krause, M. *et al.* Feedback by massive stars and the emergence of superbubbles. I. Energy efficiency and Vishniac instabilities. *A&A* **550**, A49 (2013).
- (39) Kudritzki, R.-P. & Puls, J. Winds from Hot Stars. *ARA&A* **38**, 613–666 (2000).
- (40) Maeder, A. *Physics, Formation and Evolution of Rotating Stars* (Springer Berlin, Heidelberg, 2009).
- (41) Maeder, A. & Meynet, G. The Evolution of Rotating Stars. *ARA&A* **38**, 143–190 (2000).
- (42) Martins, F. *et al.* On stars with weak winds: the Galactic case. *A&A* **441**, 735–762 (2005).
- (43) Massey, P. *et al.* A Modern Search for Wolf-Rayet Stars in the Magellanic Clouds: First Results. *ApJ* **788**, 83 (2014).
- (44) Mauerhan, J. C. *et al.* Red Eyes on Wolf-Rayet Stars: 60 New Discoveries via Infrared Color Selection. *AJ* **142**, 40 (2011).
- (45) Nugis, T. & Lamers, H. J. G. L. M. Mass-loss rates of Wolf-Rayet stars as a function of stellar parameters. *A&A* **360**, 227–244 (2000).
- (46) Obst, A. W. & Braithwaite, W. J. Measurement of the radiative branching ratio for the 7.65-MeV state in ^{12}C using the cascade gamma decays. *Phys. Rev. C* **13**, 2033–2043 (1976).
- (47) Padmanabhan, T. *Theoretical Astrophysics - Volume 1, Astrophysical Processes* (2000).
- (48) Payne, C. H. *Stellar Atmospheres; a Contribution to the Observational Study of High Temperature in the Reversing Layers of Stars*. PhD thesis (1925).
- (49) Péroux, C. & Howk, J. C. The Cosmic Baryon and Metal Cycles. *ARA&A* **58**, 363–406 (2020).
- (50) Puls, J. *et al.* Radiation driven winds of hot luminous stars. XIV. Line statistics and radiative driving. *A&AS* **141**, 23–64 (2000).

- (51) Puls, J. *et al.* Mass loss from hot massive stars. *A&A Rv* **16**, 209–325 (2008).
- (52) Richer, H. B. *et al.* Probing the Faintest Stars in a Globular Star Cluster. *Science* **313**, 936–940 (2006).
- (53) Salpeter, E. E. The Luminosity Function and Stellar Evolution. *ApJ* **121**, 161 (1955).
- (54) Sana, H. *et al.* Binary Interaction Dominates the Evolution of Massive Stars. *Science* **337**, 444 (2012).
- (55) Schweyer, T. *et al.* SN 2019odp: A Massive Oxygen-Rich Type Ib Supernova. *arXiv e-prints*, arXiv:2303.14146 (2023).
- (56) Smartt, S. J. Progenitors of Core-Collapse Supernovae. *ARA&A* **47**, 63–106 (2009).
- (57) Smith, R. *et al.* Precision measurements on oxygen formation in stellar helium burning with gamma-ray beams and a Time Projection Chamber. *Nature Communications* **12**, 5920 (2021).
- (58) Sylvester, R. J. *et al.* Silicate and hydrocarbon emission from Galactic M supergiants. *MNRAS* **301**, 1083–1094 (1998).
- (59) Van Loon, J. T. *et al.* Mass-loss rates and luminosity functions of dust-enshrouded AGB stars and red supergiants in the LMC. *A&A* **351**, 559–572 (1999).
- (60) Vink, J. S. Winds from stripped low-mass helium stars and Wolf-Rayet stars. *A&A* **607**, L8 (2017).
- (61) Vink, J. S. Theory and Diagnostics of Hot Star Mass Loss. *ARA&A* **60**, 203–246 (2022).
- (62) Vink, J. S. *et al.* Mass-loss predictions for O and B stars as a function of metallicity. *A&A* **369**, 574–588 (2001).
- (63) Virtanen, P. *et al.* SciPy 1.0: fundamental algorithms for scientific computing in Python. *Nature Methods* **17**, 261–272 (2020).
- (64) Wagle, G. A. *et al.* Type IIP Supernova Progenitors. III. Blue to Red Supergiant Ratio in Low-metallicity Models with Convective Overshoot. *ApJ* **894**, 118 (2020).
- (65) Wu, S.-W. *et al.* The massive stellar population of W49: A spectroscopic survey. *A&A* **589**, A16 (2016).

APPENDIX A

DATA TABLES

This appendix contains tables of data that was created as part of the analysis of the models and used in the discussion somewhere in the main body. The data represented here is also partly shown in the figures and can be used for cross-checking.

The tables begin on the following page.

$M_{\text{ini}} [M_{\odot}]$	\dot{M}_{OB}	\dot{M}_{RSG}	$\langle \log \dot{M}_{\text{OB}} \rangle$	$\delta \log \dot{M}_{\text{OB}}$	$\langle \log \dot{M}_{\text{RSG}} \rangle$	$\delta \log \dot{M}_{\text{RSG}}$
20	Vin01	Cro01	-7.39	0.12	-4.80	0.03
25			-6.90	0.11	-4.49	0.05
30			-6.56	0.11	-4.16	0.07
40			-6.12	0.10	-3.75	0.08
20		Bea20	-7.39	0.12	-6.27	0.07
25			-6.90	0.11	-6.32	0.06
30			-6.56	0.11	-6.59	0.03
40			-6.12	0.10	-7.74	0.04
50		–	-5.78	0.20	na	na
60			-5.51	0.33	na	na
66			-5.40	0.32	na	na
73			-5.28	0.31	na	na
80			-5.17	0.31	na	na
85			-5.11	0.32	na	na
95			-5.01	0.31	na	na
105			-4.94	0.29	na	na
120			-4.83	0.26	na	na
20	Bjo22	Cro01	-8.27	0.19	-4.73	0.03
25			-7.72	0.18	-4.39	0.05
30			-7.32	0.17	-4.11	0.06
40			-6.75	0.14	-3.69	0.09
20		Bea20	-8.27	0.19	-6.15	0.08
25			-7.72	0.18	-6.15	0.05
30			-7.32	0.17	-6.42	0.03
40			-6.75	0.14	-7.52	0.04
50		–	-6.36	0.11	na	na
60			-6.07	0.09	na	na
66			-5.93	0.08	na	na
20	Bes20	Cro01	-8.24	0.22	-4.74	0.03
25			-7.74	0.26	-4.40	0.05
30			-7.38	0.27	-4.12	0.06
40			-6.87	0.28	-3.69	0.08
20		Bea20	-8.24	0.22	-6.18	0.08
25			-7.74	0.26	-6.15	0.05
30			-7.38	0.27	-6.46	0.03
40			-6.87	0.28	-7.54	0.04
50		–	-6.52	0.28	na	na
60			-6.25	0.27	na	na
66			-6.12	0.27	na	na
73			-5.99	0.26	na	na
80			-5.88	0.26	na	na
85			-5.80	0.25	na	na
95			-5.67	0.24	na	na
105			-5.55	0.24	na	na
120			-5.40	0.23	na	na

Table A.1: Time-averaged mass loss rates obtained during the validity domains of the \dot{M}_{OB} prescriptions (main sequence only), as well as the \dot{M}_{RSG} prescriptions, with standard deviations. Units of mass loss rates are solar masses per year. This data shown in [Figure 4.2](#) and [Figure 4.3](#).

$M_{\text{ini}} [M_{\odot}]$	\dot{M}_{OB}	\dot{M}_{RSG}	$M [M_{\odot}]$	$\log(T_{\text{eff}}[\text{K}])$	$\log(L/L_{\odot})$	Γ_{Edd}	X_{s}	$\tau_{\text{MS}} [\text{Myr}]$
20	Vin01	Cro01	19.7	4.47	5.00	0.134	0.720	7.89
25			24.2	4.48	5.23	0.186	0.720	6.33
30			28.5	4.48	5.40	0.233	0.720	5.49
40			36.5	4.45	5.63	0.312	0.720	4.47
20		Bea20	19.7	4.47	5.00	0.134	0.720	7.89
25			24.2	4.48	5.23	0.186	0.720	6.33
30			28.5	4.48	5.40	0.233	0.720	5.49
40			36.5	4.45	5.63	0.312	0.720	4.47
50		–	42.2	4.36	5.79	0.390	0.720	3.90
60			36.4	4.39	5.90	0.499	0.502	3.55
66			39.9	4.41	5.96	0.521	0.475	3.39
73			43.7	4.43	6.03	0.543	0.441	3.24
80			47.1	4.46	6.09	0.564	0.401	3.11
85			49.5	4.48	6.13	0.575	0.376	3.04
95			54.0	4.52	6.20	0.594	0.328	2.91
105			59.2	4.53	6.26	0.614	0.303	2.81
120			63.3	4.65	6.33	0.625	0.208	2.68
20	Bjo22	Cro01	20.0	4.47	5.01	0.136	0.720	7.84
25			24.9	4.48	5.25	0.190	0.720	6.24
30			29.7	4.49	5.43	0.241	0.720	5.42
40			39.2	4.47	5.68	0.324	0.720	4.37
20		Bea20	20.0	4.47	5.01	0.136	0.720	7.84
25			24.9	4.48	5.25	0.190	0.720	6.24
30			29.7	4.49	5.43	0.241	0.720	5.42
40			39.2	4.47	5.68	0.324	0.720	4.37
50		–	48.3	4.46	5.85	0.387	0.720	3.81
60			57.0	4.42	5.98	0.440	0.720	3.45
66			60.6	4.33	6.03	0.472	0.720	3.30
20	Bes20	Cro01	19.8	4.47	5.00	0.135	0.720	7.84
25			24.6	4.48	5.25	0.190	0.720	6.25
30			29.4	4.48	5.43	0.241	0.720	5.41
40			38.5	4.45	5.68	0.326	0.720	4.37
20		Bea20	19.8	4.47	5.00	0.135	0.720	7.84
25			24.6	4.48	5.25	0.190	0.720	6.25
30			29.4	4.48	5.43	0.241	0.720	5.41
40			38.5	4.45	5.68	0.326	0.720	4.37
50		–	47.2	4.42	5.85	0.395	0.720	3.80
60			55.2	4.34	5.98	0.452	0.720	3.44
66			59.7	4.26	6.04	0.484	0.720	3.28
73			60.0	3.87	6.09	0.538	0.698	3.13
80			52.1	4.21	6.14	0.591	0.449	3.01
85			55.2	4.23	6.18	0.602	0.430	2.94
95			61.4	4.24	6.25	0.622	0.400	2.82
105			67.5	4.25	6.31	0.640	0.371	2.72
120			76.1	4.28	6.39	0.660	0.329	2.60

Table A.2: Properties of the models at the terminal-age main sequence (TAMS), discussed in [section 4.2](#).

$M_{\text{ini}} [M_{\odot}]$	\dot{M}_{OB}	\dot{M}_{RSG}	$M [M_{\odot}]$	$\log(T_{\text{eff}}[\text{K}])$	$\log(L/L_{\odot})$	Γ_{Edd}	Age [Myr]
20	Vin01	Cro01	na	na	na	na	na
25			na	na	na	na	na
30			10.3	4.36	5.44	0.538	1.108
40			14.6	4.60	5.57	0.506	1.089
20		Bea20	na	na	na	na	na
25			na	na	na	na	na
30			na	na	na	na	na
40			na	na	na	na	na
50		–	19.6	4.74	5.75	0.571	1.074
60			28.0	4.00	6.01	0.638	1.005
66			31.7	4.00	6.07	0.647	1.004
73			35.7	4.01	6.13	0.664	1.003
80			41.2	4.00	6.20	0.675	1.002
85			42.3	4.00	6.22	0.693	1.003
95			48.1	4.00	6.29	0.709	1.002
105			59.1	4.36	6.28	0.650	1.001
120			68.7	4.44	6.31	0.597	0.973
20	Bjo22	Cro01	na	na	na	na	na
25			8.7	4.01	5.39	0.551	1.124
30			10.9	4.02	5.61	0.613	1.116
40			15.7	4.14	5.67	0.597	1.105
20		Bea20	na	na	na	na	na
25			na	na	na	na	na
30			na	na	na	na	na
40			na	na	na	na	na
50		–	20.5	4.57	5.80	0.616	1.090
60			25.4	4.56	5.91	0.638	1.064
66			28.5	4.32	5.97	0.663	1.059
20	Bes20	Cro01	na	na	na	na	na
25			na	na	na	na	na
30			10.8	4.07	5.53	0.584	1.109
40			15.7	4.48	5.63	0.544	1.097
20		Bea20	na	na	na	na	na
25			na	na	na	na	na
30			na	na	na	na	na
40			na	na	na	na	na
50		–	20.5	4.72	5.78	0.591	1.074
60			25.7	4.60	5.91	0.632	1.057
66			29.1	4.43	5.98	0.656	1.051
73			36.6	4.00	6.11	0.664	1.007
80			43.7	4.00	6.23	0.690	1.002
85			47.6	4.01	6.27	0.694	1.002
95			52.9	4.00	6.33	0.715	1.002
105			59.4	4.00	6.38	0.729	1.002
120			68.5	4.00	6.46	0.749	1.002

Table A.3: Properties of the models when they enter the Wolf-Rayet (WR) phase, as shown in [Figure 4.12](#).

$M_{\text{ini}} [M_{\odot}]$	M_{OB}	\dot{M}_{RSG}	$M [M_{\odot}]$	$\log(T_{\text{eff}}[\text{K}])$	$\log(L/L_{\odot})$	Type	X_{s}	Y_{s}	$Z_{\text{s}}(^{12}\text{C})$	$M_{\text{CO}} [M_{\odot}]$	Age [Myr]
20	Vin01	Cro01	8.9	3.57	5.18	RSG	0.487	0.499	0.000	3.8	8.81
25			na	na	na	na	na	na	na	na	na
30			10.1	4.70	5.51	WN	0.000	0.986	0.000	7.2	6.09
40			na	na	na	na	na	na	na	na	na
20		Bea20	17.2	3.56	5.19	RSG	0.616	0.370	0.001	4.0	8.93
25			19.5	3.57	5.38	RSG	0.550	0.436	0.001	5.5	7.06
30			27.2	3.60	6.09	RSG	0.571	0.415	0.001	7.6	6.10
40			36.1	3.58	5.88	RSG	0.532	0.454	0.001	11.5	4.96
50		–	16.6	5.37	5.87	WO	0.000	0.199	0.450	13.2	4.33
60			12.9	5.35	5.69	WO	0.000	0.273	0.510	10.0	3.95
66			14.2	5.37	5.77	WO	0.000	0.267	0.505	11.2	3.78
73			15.8	5.37	5.84	WO	0.000	0.260	0.499	12.6	3.61
80			17.9	5.37	5.93	WO	0.000	0.253	0.492	na	3.48
85			18.8	5.37	5.96	WO	0.000	0.248	0.488	15.1	3.39
95			21.4	5.36	6.04	WO	0.000	0.240	0.479	17.3	3.25
105			24.2	5.34	6.11	WO	0.000	0.236	0.470	19.7	3.14
120			28.4	5.28	6.21	WO	0.000	0.229	0.458	23.4	3.00
20	Bjo22	Cro01	13.4	3.56	5.20	RSG	0.571	0.415	0.001	4.0	8.75
25			8.6	4.52	5.45	WN	0.060	0.926	0.000	5.8	7.02
30			10.8	4.54	5.59	WN	0.000	0.986	0.000	7.7	6.05
40			na	na	na	na	na	na	na	na	na
20		Bea20	18.8	3.56	5.20	RSG	0.626	0.360	0.001	3.9	8.75
25			22.7	3.57	5.44	RSG	0.585	0.401	0.001	5.8	6.94
30			28.3	3.58	5.59	RSG	0.564	0.422	0.001	7.9	6.00
40			38.8	3.58	5.79	RSG	0.524	0.462	0.001	12.2	4.84
50		–	18.3	5.36	5.94	WO	0.000	0.124	0.372	14.3	4.24
60			19.7	5.37	5.99	WO	0.000	0.271	0.474	15.9	3.84
66			21.3	5.36	6.04	WO	0.000	0.256	0.475	17.3	3.67
20	Bes20	Cro01	12.3	3.56	5.20	RSG	0.556	0.431	0.001	4.0	8.77
25			8.6	3.83	5.40	YSG	0.209	0.777	0.000	5.8	6.96
30			10.8	4.62	5.57	WN	0.007	0.980	0.000	7.6	6.01
40			na	na	na	na	na	na	na	na	na
20		Bea20	18.7	3.56	5.22	RSG	0.626	0.360	0.001	3.9	8.77
25			22.4	3.57	5.20	RSG	0.583	0.403	0.001	5.8	6.95
30			28.2	3.57	5.49	RSG	0.566	0.420	0.001	7.9	6.00
40			38.2	3.58	5.82	RSG	0.515	0.471	0.001	12.2	4.84
50		–	17.8	5.37	5.92	WO	0.000	0.205	0.458	14.0	4.22
60			20.7	5.37	6.02	WO	0.000	0.231	0.473	16.8	3.82
66			22.7	5.36	6.08	WO	0.000	0.251	0.473	18.5	3.65
73			23.8	5.34	6.10	WO	0.000	0.233	0.470	19.4	3.48
80			27.6	5.29	6.19	WO	0.000	0.226	0.458	22.6	3.35
85			29.2	5.26	6.22	WO	0.000	0.224	0.452	24.1	3.27
95			32.9	5.13	6.28	WC	0.000	0.222	0.443	27.4	3.14
105			36.9	4.09	6.34	WC	0.000	0.218	0.432	31.1	3.03
120			42.7	4.03	6.42	WC	0.000	0.213	0.419	36.4	2.90

Table A.4: Properties of the models at the end of central carbon burning, discussed in section 4.4, with data shown in Figure 4.14, Figure 4.15, Figure 4.16 and Figure 4.17.

APPENDIX B

ANALYTICAL DERIVATION OF STELLAR SCALING RELATIONS

Here I present an analytical derivation of some important stellar scaling relations, for example the mass-luminosity relation. As a starting point, we use the stellar structure equations as well as the equation of state for an ideal gas, as presented in [Chapter 3](#).

The main idea in these derivations is to approximate derivatives as difference quotients and to omit all constants in order to highlight how fundamental quantities scale with respect to each other. Furthermore, we take $r \sim R$, $M_r \sim M$ and $L_r \sim L$, since these variables are of the order of magnitude of their surface values in most of the star.

To start, the density is $\rho \sim M/R^3$. According to the second stellar structure equation (hydrostatic equilibrium), and postulating that the surface pressure is zero, we obtain for the central pressure P_c :

$$\frac{P_c}{R} \sim \rho \frac{M}{R^2} \sim \frac{M}{R^3} \frac{M}{R^2} \Rightarrow \boxed{P_c \sim \frac{M^2}{R^4}} \quad (\text{B.1})$$

Combining this result with the ideal gas EOS, and taking β as the ratio between gas pressure and total pressure, we obtain for the central temperature T_c :

$$P_c = \frac{P_{c,\text{gas}}}{\beta} \stackrel{\text{EOS}}{\sim} \frac{\rho T_c}{\mu \beta} \Rightarrow \boxed{T_c \sim \frac{M \mu \beta}{R}} \quad (\text{B.2})$$

The fourth stellar structure equation (radiative transfer) gives us an alternative way to estimate the central temperature. From this equation, assuming the surface temperature is negligible compared to T_c , we obtain:

$$\frac{T_c}{R} \sim \frac{\kappa \rho}{T_c^3} \frac{L}{R^2} \Rightarrow \boxed{T_c^4 \sim \frac{\kappa M L}{R^4}} \quad (\text{B.3})$$

Combining the last two results we obtain a relation for the luminosity:

$$\boxed{L \sim \frac{M^3 \mu^4 \beta^4}{\kappa}} \quad (\text{B.4})$$